2022

Using deep learning to assess new bone formation after bone grafting

BOSTON UNIVERSITY

HENRY M. GOLDMAN SCHOOL OF DENTAL MEDICINE

THESIS

**USING DEEP LEARNING TO ASSESS NEW BONE FORMATION AFTER
BONE GRAFTING**

by

ELIAS A. EXARCHOS

B.S. Biomedical Engineering, Boston University, 2015
D.M.D., Boston University, 2019

Submitted in partial fulfillment of the requirements for the degree of

Master of Science in Dentistry
In the Department of Periodontology

2022

Approved by:

First Reader   _____
                Taisuke Ohira, DDS, PhD
                Clinical Assistant Professor, Department of Periodontology

Second Reader   _____
                Wayne A. Gonnerman, PhD
                Assistant Professor, Department of Periodontology

Third Reader   _____
                Serge Dibart, DMD
                Chair, Department of Periodontology

DEDICATION

I would like to dedicate this work to my patient wife, my loving mother who has always supported me, and my father who has always inspired me and encouraged me to never give up, no matter what.

ACKNOWLEDGMENTS

USING DEEP LEARNING TO ASSESS NEW BONE FORMATION AFTER BONE GRAFTING

ELIAS A. EXARCHOS

Boston University, Henry M. Goldman School of Dental Medicine, 2022

Major Professor: Taisuke Ohira, DDS, PhD

Clinical Assistant Professor of Periodontology

ABSTRACT

Background: The ultrasonic vibrations from the piezoelectric knife may amplify the natural response to surgical injury. This may lead to different clinical and biological outcomes when using the piezoelectric knife versus a surgical bur to create selective cortical penetrations for alveolar ridge augmentation surgeries. The first aim of this study was to analyze the differences in bone graft healing when selective cortical penetrations are created with a surgical bur and with a piezoelectric knife. The second aim of this pilot study was to see if enhanced new bone formation during bone regeneration procedures can be achieved with the use of a piezoelectric knife versus the conventional bur or onlay grafting techniques utilizing deep learning, a subset of machine learning.

Materials & Methods: he project was approved by the Boston University Medical Center Institutional Animal Care and Use Committee (IACUC). Twenty, 9-10 week male Sprague Dawley rats, weighing approximately 300g, were used in this study. The rats

were randomly divided into three groups: *Xenograft*, *Alloplast*, and *Collagen*. These groups were further divided by surgical technique: *Bur*, *Piezo*, and *Onlay*. For the Bur and Piezo groups, four equally-spaced selective cortical penetrations were made prior to bone graft stabilization. Three rats served as controls (*Control* group). Microcomputed tomography scans (*μCT*) were acquired for each sample, containing approximately 1,000 slices of data each. After 28 days of healing the volumes of and density of the newly formed bone were extracted and analyzed for each group. This was achieved with an innovative deep learning algorithm designed for multi-level segmentation and regional feature detection utilizing convolutional neural networks (*CNN*).

Results: Microcomputed tomography (μCT) of our samples yielded very localized, high-resolution scans of our surgical samples. The innovative deep learning algorithm was able to reliably produce highly accurate, unbiased segmentations of our samples. This study demonstrated that new bone formation was possible with all nine of the tested surgical techniques, however the differences were not statistically significant. Selective cortical penetrations with a piezoelectric knife (*PIEZO*) resulted in significantly more "cortical-like" new bone formation at 28 days.

Conclusion: Within the limitations of this preliminary study, it is possible to conclude that the piezoelectric knife is a valid alternative to conventional carbide burs when making selective cortical penetrations prior to bone grafting surgery. Additionally, our deep learning algorithm successfully segmented thousands of slices of data and allowed for the calculation of porosity and new bone volume in our samples.

TABLE OF CONTENTS

LIST OF TABLES

LIST OF FIGURES

LIST OF ABBREVIATIONS

μCT .... Micro-Computed Tomography

ADO .... Alveolar Distraction Osteogenesis

AI .... Artificial Intelligence

BMU .... Basic Multicellular Unit

BU .... Boston University

FOV... Field of View

GBR .... Guided Bone Regeneration

ISO .... International Standards Organization

MSC .... Mesenchymal Stem Cell

RANK-L .... Receptor Activator or Nuclear Factor kappa-B Ligand

RAP.. Regional Acceleratory Phenomenon

rhPDGF-BB .... recombinant human Platelet-Derived Growth Factor-BB

ROI..Region of Interest

SCP .... Selective Cortical Penetrations

SMART.......Subperiosteal Minimally Invasive Aesthetic Ridge Augmentation Technique

TGF-β.. Transforming Growth Factor β

CHAPTER 1

INTRODUCTION

1.1 Bone Grafting in Periodontology

Advancements in the field of implant dentistry have given rise to various

materials and methods designed to avoid alveolar ridge augmentation. However,

clinicians still often encounter situations where inadequate maxillary or mandibular bone

volume inhibits the esthetic or functional placement of dental implants. These alveolar

bone deficiencies can be caused by periodontal disease, alveolar resorption subsequent to

tooth loss, trauma, long-term use of a removable prosthesis, pathology, or congenital

defects. [1] [2] [3]

Adequate volume of alveolar bone, the main requirement for successful long-term

dental implants, can be restored in the edentulous alveolar ridge through various surgical

procedures. Several ridge augmentation techniques, e.g. guided bone regeneration (GBR),

ridge splitting and expansion, and autologous bone block grafting, have been tested

extensively and shown to predictably augment bone height and width. [4] Although these

procedures are usually successful, each hard tissue augmentation procedure has

advantages and disadvantages. And, each patient's treatment plan should be tailored

based on a fundamental understanding of the literature, both current and classic, and the

biology and anatomy of dentoalveolar bone.

1.2 Types of Bone Grafts

Bone grafts used in dentistry develop bone through three possible mechanisms: direct osteogenesis, osteoconduction, and osteoinduction. Grafts may regenerate bone from one, two, or all three of these mechanisms to varying degrees. [5]

A. *Osteoconductive*: Graft material does not directly contribute to new bone formation but serves as a scaffold for bone formation by adjacent host bone.

B. *Osteoinductive*: Bone formation is induced in the surrounding soft tissue immediately adjacent to the grafted material.

C. *Osteogenic*: New bone formation occurs as a result of bone-forming cells contained in the graft.

Osteoconduction supports the attachment of osteoblasts and osteo-progenitor cells and to allow the migration and ingrowth of these cells within the three-dimensional architecture of the graft. [6] Osteoinduction means that the graft can induce the primitive, undifferentiated and pluripotent cells to develop into the bone-forming cell-lineage, by which osteogenesis is induced. [7] Osteogenesis allows osteodifferentiation and subsequent new bone formation occurs through donor cells derived from either the host or the grafts. [8] [9] Different bone grafting materials have been used in dentistry with the purpose of replacing/grafting of human bone, but each product/material has its own particular advantages and disadvantages, and they are classified as being either *autografts*, *allografts*, *xenografts*, or *alloplasts*. [10]

1.2.1 Autografts

Autogenous grafts are transferred from one position to another within the same individual. In periodontology and oral surgery, this means that a second surgical site is needed (e.g., retromolar pad, maxillary tuberosity). Autogenous grafts are also known as autografts and are the gold standard to which all other grafting materials are compared because they possess all the previously mentioned healing mechanisms (osteogenicity, osteoinductivity, and osteoconductivity). In addition, because they are from the same individual, they obviate graft-host reactions mediated by histocompatibility mismatches because of the absence of antigenicity. [11]

For the purpose of this animal study, autografts were not part of the experimental model because of the difficult and complex surgery required to harvest such grafts.

1.2.2 Allografts

Allografts, also called allogenic, homologous, or homografts, are composed of materials taken from genetically dissimilar members of the *same species*. Allografts are histocompatible and are available in various forms, including demineralized bone matrices, cancellous chips, cortico-cancellous grafts, cortical grafts, and osteochondral or whole-bone segments, depending on the host's requirements. Although viable cells are lacking, allogenic bone grafts provide similar mechanical properties as the autologous

bone grafts, and it may also contain the collagenous matrix/network and proteins of natural bone. [12]

Since this study was conducted on Sprague-Dawley rats, allografts were not included in the experimental model simply because there are no commercially available bone grafts derived from this species.

1.2.3 Xenografts

Xenografts, also known as heterografts or xenogenic grafts, are from donors of another species. Several studies have shown successful hard tissue regenerative outcomes with xenogenic grafts and they hold a major role in dental, periodontal, and cranio-maxillofacial applications. In randomized controlled clinical trials [13] [14] a bovine xenograft or a synthetic bone substitute both presented similar radiographic alveolar bone changes when used for alveolar ridge preservation procedures or ridge augmentation procedures adjacent to dental implant implants. [15]

A xenogenic bone graft (Bio-Oss Collagen) was used for this animal study (*Xenograft* study group). Bio-Oss Collagen is a mixture of spongiosa (cancellous) bovine bone granulate (xenograft) and porcine collagen fibers. The material is 10% Type I collagen by volume. It is an allergen-free bone substitute and several histologic and histomorphometric studies have shown that it can successfully form lamellar, parallel-

fiber, and woven bone. [16] This bovine xenograft seems to resorb very slowly in humans compared to other bone graft materials and residual particles are usually present for long periods of time in close/intimate contact with the newly formed native bone and osteoid tissue.

1.2.4 Alloplasts

Alloplasts, also known as alloplastic or synthetic grafts, are artificial or manufactured materials used as a substitute for natural bone graft materials and can be subdivided based on their origin and chemical composition. Alloplastic bone graft materials include calcium sulfates, hydroxyapatites, tricalcium phosphates, calcium phosphate cements/ceramics, and bioactive glass. [17] Although they lack osteoinductive or osteogenic properties, synthetic bone substitutes are in increasing demand as the aging population increases. Moreover, they have demonstrated the promising potential to be biomaterials for bone tissue engineering due to their controllable and tunable biomechanical and biodegradability properties. [18] Also, they provide better controllability in terms of porosity, physiochemical structure and immunologic adverse effects when compared to other types of bone grafting materials. [19] [20]

For this study, in addition to a xenograft study group, a non-sintered, resorbable calcium apatite-based *Alloplast* bone graft material (OsteoGen) was used. These calcium apatite crystals are embedded in Type I bovine Achilles tendon cartilage. The final

product is easy to handle as it comes pre-made in a pliable sheet that simplifies the

preparation, application, and delivery of the graft material (OsteoGen Strips). These

"strips" address the clinical need for a synthetic bone substitute and have been used

extensively in extraction socket grafting and immediate implant-related bone grafting

procedures. It was approved for use by the FDA in 2009 [21] and what is unique about

this material is the low temperature preparation technique. This non-sintered product uses

a low-temperature manufacturing process (so as to not distort the physical form of the

crystal) that generates osteoconductive and resorbable low-density crystals and crystal

clusters with distinctive calcium to phosphate ratios that makes it neither a beta-

tricalcium phosphate nor a dense non-resorbable ceramic hydroxyapatite. [22] [23]

1.2.5 Other

A third "bone grafting material" was tested in this study and it is not an autograft,

an allograft, a xenograft, nor an allograft. It is not classified as a "bone graft"; it is a

collagen matrix (*Collagen* study group). Geistlich's Mucograft provides short-term

volume-stability and cell-occlusive properties. And we tested whether or not this could

maintain the subperiosteal space long enough for new bone formation to occur when used

in conjunction with selective cortical penetrations (SCPs). [24]

Mucograft is a resorbable porcine collagen matrix with two structures: a compact

layer for tissue adherence (for favorable wound healing) and a thick spongious

layer/scaffold which facilitates and promotes formation of new blood vessels, a key requirement for soft/hard tissue regeneration healing. Mucograft has mostly been tested as a barrier membrane or alongside soft tissue augmentation procedures. It has been shown to result in minimal inflammation, an absence of multinucleated giant cells, and favorable tissue reactivity profiles.[25] It is an easy-to-handle material and can be purchased in matrices of varying sizes and shapes. Per the manufacturer, there is no need for preoperative hydration, which can also reduce chairside time. [26] [27]

1.3 Surgical Techniques

GBR is not the only hard tissue augmentation method used in periodontal and oral surgery. Several studies have demonstrated successful new bone formation with other techniques as well such as: distraction osteogenesis, block grafting, ridge splitting, maxillary sinus lifting, and onlay grafting without the use of a cell-occlusive membrane.

1.3.1 GBR

Guided bone regeneration (GBR) is a surgical procedure that has been used for several years to augment alveolar bone height and/or width, in preparation for dental implant placement. This surgical procedure involves: (1) reflecting a full-thickness flap, (2) placing a bone graft against the underlying bony defect, and (3) fixing a resorbable or non-resorbable membrane over the bone graft. This thereby creates and maintains a space

under the periosteum for new bone formation to occur, while preventing non-osteogenic cells from interfering with the desired new bone growth. [3]

Ideally, for new bone regeneration, osteoprogenitor cells should colonize this space, however these cells grow slowly. In order to give the osteoprogenitor cells the ability to colonize this space, the cell-occlusive membrane used in GBR prevents the ingrowth of the rapidly proliferating epithelial and connective tissue cells into the defect. [4] This careful inclusion and exclusion of specific cells inside and away from the graft space is one of the fundamental reasons why clinicians have had very high long-term success rates with guided bone regeneration.

1.3.2 Distraction Osteogenesis

Alveolar distraction osteogenesis (ADO) is a bone regeneration technique based on a biological process used for regenerating and consolidating bone between two bone segments obtained after initial osteotomy. [28] These segments are gradually separated by the process of distraction and this technique (device) can achieve increased new bone volume in both horizontal and vertical dimensions. [29] [30]

1.3.3 Ridge Splitting and Expansion

Ridge splitting is a technique used to augment the alveolar ridge prior to (or simultaneously with) dental implant placement. This technique involves cutting the

cortical plate(s) deep enough into the marrow space and creating a "hinge"-like attached

plate of bone that can be split and spread from the opposing wall, without being fully

removed. Due to the need to enter marrow space, this technique requires special attention

to the density of the bone, the distance to neighboring teeth/vital structures, and sufficient

width of the original bone itself. An inlay graft (either particulate or block) is usually

"sandwiched" between the two plates of bone in order to maintain the space. Several

ridge split techniques have been developed in the past few decades and they include, but

are not limited to, the split crest osteotomy [31] [32] and the ridge expansion osteotomy.

[33]

1.3.4 Maxillary Sinus Lift

Maxillary sinus lifts are commonly used in periodontology and oral surgery to

augment the hard tissue volume prior to implant placement in the posterior maxillary

region(s). It involves separating the Schneiderian membrane from the internal walls of

the maxillary sinuses and condensing a volume-stable grafting material underneath the

periosteal space(s), allowing time for new bone formation to occur. The conventional

method for maxillary sinus elevation ("direct sinus lifts") requires surgical access through

the lateral wall of the maxilla, followed by elevation of the sinus membrane and insertion

of bone graft under *direct* vision. [34] [35] A modified less invasive method uses a crestal

approach *without direct* vision of the Schneiderian membrane ("indirect sinus lift"). [36]

These techniques do not usually require the use of a cell-occlusive membrane as long as

the Schneiderian membrane is not ruptured, and the overlaying periosteum is remained intact.

Variations of this type of technique have shown potential for new bone formation even without a bone graft in the maxillary sinus. This has been described in a variety of studies, including radiological and histological studies, and the recent studies on this topic indicate high success rates of maxillary sinus lifts without a bone graft material. A literature review by Pinchasov *et al*. concluded that the evidence clearly shows that the maxillary sinus has the potential to heal and form new bone without bone grafts or substitutes. [37] A recent meta-analysis performed by Yan *et al.* demonstrated that the available evidence suggests that predictable results can be acquired through transalveolar sinus floor lift without bone grafting, however there may be a trend towards more new bone formation with the use of bone grafts. [38]

1.3.5 Subperiosteal Onlay Grafts

Onlay grafting (without the use of a membrane) is a hard tissue regeneration method that utilizes particulate bone grafting material underneath an *intact* periosteal surface. If the periosteum is carefully maintained intact during full-thickness flap elevation, this can serve as a barrier to the migration of epithelial and soft tissue connective tissue cells, allowing new bone formation to ensue. [39] Plus, the minimally invasive nature of this method (without disrupting the soft tissues overlying the recipient

bed) results in minimal surgical trauma, postoperative discomfort, and morbidity. A number of variations of subperiosteal tunneling have been reported and they have shown successful ridge augmentation volume gains with the use of particulate hydroxyapatite and human mineralized bone allograft. [40] [41] Selective cortical penetrations of the recipient site(s), also known as "decortication", have been recommended in conjunction with anorganic bovine bone particulate grafts when hard tissue regeneration is desired beneath subperiosteal tunnels/pouches. [42]

Dibart *et al.* reported on the use of subperiosteal tunneling with bone grafting and piezosurgical corticotomies as an adjunct to surgically facilitated orthodontic therapy. [43] Nevins *et al.* compared and reported variable outcomes with the use of recombinant human platelet-derived growth factor BB (rhPDGF-BB) in combination with three different particulate bone matrices (freeze-dried bone allograft (FDBA), anorganic bovine bone graft (ABBG), or anorganic bovine bone graft/mineralized collagen bone substitute (ABBG/MCBS)) for the treatment of maxillary anterior edentulous spaces. [44]

The MIHRA technique is a similar technique that uses a small incision and subperiosteal tunneling (Minimal Invasive Horizontal Ridge Augmentation) and has been tested with various bone graft materials (autograft, allograft, and xenograft). [45] Significant bone gain has been reported and grafting underneath an intact periosteal pouch has proven to be a valid, safe, simple, and effective method of reconstructing hard tissue defects.

Recently, Dr. Ernesto Lee has published and trademarked the "SMART" method (Subperiosteal Minimally Invasive Aesthetic Ridge Augmentation Technique). His technique involves making one or more small access incisions, reflecting a full-thickness subperiosteal pouch, and placing xenograft (bovine) particles mixed with GEM21S (rhPDGF-BB) onto the recipient bone without the use of SCPs (selective cortical penetrations). Histological and radiographic analyses have demonstrated that the SMART technique is a predictable, valid, and safe alternative to GBR procedures. [46] While this bone grafting technique is mostly used for lateral alveolar bone augmentation, it can be sequentially combined with orthodontic forced eruption to result in both horizontal and vertical new bone formation. [47]

Autogenous bone grafts are still considered the gold standard for predictable hard tissue volume gain. However, for subperiosteal onlay grafting, allografts, xenografts, and even alloplasts, such as various calcium phosphates, have been proven to be a valuable option for these types of bone augmentation procedures. [48] For our animal study, one allograft material and one xenograft material were chosen.

1.3.7 Bone Bioreactor

In addition to the *Allograft* group and the *Xenograft* group, a *Collagen* group was used in this study. New bone formation in an animal model has occurred under full-thickness periosteal flaps, providing that the space is *maintained* for the necessary

amount of time for the host to form new bone under the subperiosteal space. Significant

hard tissue augmentation occurs with collagen matrices and even with no grafting

material, provided that the reflected, intact periosteum provides space for new bony

growth. [49]

In 2005, Stevens *et al*. used an animal model to demonstrate that simply by

creating and manipulating an artificial space (bioreactor) between the bone and the

periosteum (a mesenchymal layer rich in pluripotent cells), the body's healing

mechanism is leveraged to engineer bone that is biomechanically identical to native bone.

Their group used a cross-linked calcium-alginate gel placed under a subperiosteal pouch

in a rabbit tibia and found that the creation of this "*in vivo* bone bioreactor" can

predictably lead to new woven bone matrix formation which matures into fully

mineralized compact bone (exhibiting all the histological markers and mechanical

properties of native bone). [24]

1.3.8 Selective Cortical Penetrations

As previously mentioned, clinicians will often decorticate the bone prior to

placing the bone graft material, with the goal of including more osteoprogenitor cells and

increasing blood supply from the marrow to the space to the graft space. However, there

is controversy in the literature regarding the effectiveness of selective cortical

penetrations on bone grafting outcomes because its ability to accelerate or increase bone

regeneration has not been substantiated in *human* clinical trials. In 2009, Greenstein *et al* did a literature review and found that there is inconsistent literature, conflicting information, and not enough clinical trials to make a definitive determination as to the merits of bone decortication prior to GBR procedures. [2] In 2008, Adeyemo *et al* found no difference in terms of healing and integration of the bone graft between perforated and nonperforated recipient cortical beds. [3]

Rompen *et al.*, however, demonstrated greater regeneration in skulls perforated with nine 0.8 mm diameter holes (172.8%) compared with skulls with an intact osseous surface (141%). It was stated that *de novo* bone formation occurs by stimulation of the blood supply and access of bone-forming cells by cortical perforations. [50] In 2017, Danesh-Sani *et al.* conducted a human study and found that, after 7 months of healing, cortical bone perforations favorably affects the amount of new bone formation, however these results were not statistically significant. They also found that cortical bone perforations significantly increased the number of new vessels (angiogenesis) of the regenerated bone. [1]

In 2018, Wessing *et al* conducted a systematic review and meta-analysis and found that decortication in GBR procedures led to an increase in alveolar ridge width, even though those values did not reach statistical significance. [51] By and large, the research generally shows better, not worse, outcomes when utilizing selective cortical penetration techniques, as the marrow space can provide greater osteoprogenitor cell

access, better blood supply, and nourishment, especially in dense mandibular bone, however these studies are not conclusive, and clinicians can choose to decorticate at their own discretion. Further human clinical trials are required to elucidate the biologically complex effects of selective cortical penetrations on bone regeneration.

When creating selective decortications in the alveolar bone, most practitioners use a conventional surgical bur with saline irrigation, however in the past, scalpels and chisels have been used. These forms of bony injuries induce something called the regional acceleratory phenomenon (RAP), a term coined in 1981 by an orthopedic surgeon, Dr. Harold M. Frost. [52] The regional acceleratory phenomenon is characterized by an increase in vascular perfusion and bone turnover as well as a decrease in bone density (transient osteopenia). This brief phase of osteopenia is quickly followed by rapid osteoblastic activity and bone remodeling, resulting in full reestablishment of bone density. Others have described the RAP as a temporary state of accelerated healing at the site of bony injury in which there is a localized increased in cellular activity and bone remodeling through the recruitment of osteoblasts and osteoclasts. [53] This type of healing following alveolar bone decortication is bimodal in nature and is thought to consist of two interrelated, overlapping phases – a demineralization phase (early phase) and a remineralization phase (later phase). [54]

Any type of bony injury of sufficient magnitude can elicit the regional acceleratory phenomenon. In the orthodontic literature, it has been shown that selective

cortical penetrations created by surgical burs, piezoelectric knives, scalpel and mallets are all able to trigger the RAP phenomenon in surgically assisted rapid orthodontic procedures. [55] [56] [57] [58] [59] Even full-thickness mucoperiosteal flap reflection alone (a type of bony injury) can initiate RAP, although the extent of this phenomenon varies depending on the intensity of the stimulus.

Of particular interest is minimally invasive technique called "Piezocision" for surgically assisted orthodontics. This technique, as mentioned previously, was introduced by Dibart *et al.* in 2009. A piezoelectric knife is used to create selective cortical penetrations in the alveolar bone to induce the regional acceleratory phenomenon for accelerated orthodontic movement. This technique involves vertical incisions that are made in the gingiva, which can also be used advantageously for tunneling procedures in which hard tissue grafts can be placed under a subperiosteal tunnel to correct bone deficiencies. [43] And, the SCPs created by the piezoelectric knife, in theory, can accelerate the bone graft healing.

Piezocision demonstrates that decortications of the alveolar bone can be made with an ultrasonic piezoelectric knife and concurrent alveolar ridge augmentations can be completed, however today, clinicians still are largely using surgical burs to create the corticotomies in alveolar bone prior to bone grafting. But why? Horton *et al* showed that osteoblastic activity and rates of healings were increased in surgical defects of alveolar bone created by ultrasonic instruments compared to a conventional rotary bur. [60] In

2013, Canullo *et al*. showed that implant stability develops faster when the implant site osteotomy is performed with a mixed drilling/piezoelectric technique versus a conventional drilling technique. [60] And, in 2018, Fugito *et al.* demonstrated that the use of either piezoelectric tips or rotary burs generates a temperature that does not affect the healing hard/soft tissues. [62] Lastly, in 2019, Alikhani *et al* demonstrated that locally applied, high frequency vibrations, similar to those used in piezoelectric instruments, stimulates alveolar bone formation under physiologic conditions and that these locally applied vibrations can generate gradients of increased anabolic metabolism and decreased catabolic metabolism in alveolar bone. [63]

Therefore, it is conceivable that the choice to utilize a conventional surgical carbide bur or a piezoelectric knife and the choice to create selective cortical penetrations whatsoever in conjunction with bone regeneration procedures may lead to quantitative and qualitative differences in new bone formation due to the differences in tissue damage and tissue response. So, for our experiment, we further subdivided our study groups into a *Bur* group, a *Piezo* group, and an *Onlay* group with no SCPs.

1.4 Biological Background

With regards to augmenting missing hard tissue in the oral cavity or craniofacial region, basic knowledge of the bone anatomy is crucial in order to appreciate the particulars of various bone augmentation techniques. The maxilla and mandible, like most bones of the skull, are formed embryologically through intramembranous

ossification. [64] Developing alveolar bone becomes a highly mineralized tissue and, like bone in other parts of the human skeleton, has a matrix consisting of organic matter (mostly type I collagen and other proteins), inorganic matter (calcium phosphate in the form of hydroxyapatite crystals), and cells. [5] There is a dynamic relationship between these hard tissues and the cells, vasculature, and soft tissues that surround the mandibular and maxillary bone.

1.4.2 Periosteum

The outermost layer of the bone comprises the periosteum. The periosteum is a dense layered membrane responsible for partial blood supply to bone and bone fracture repair. In fact, 18th century surgeons discovered that the periosteum is capable of inducing new bone formation. [65] The first layer of the periosteum is an outer fibrous layer providing physical and structural support. The inner cambium layer contains many osteoprogenitor cells. However, the thickness of the cambium osteoprogenitor layer decreases with age, concomitant with a decrease in its osteogenic potential. [66] In some bones, there is also an endosteum. This endosteal membrane is derived from the periosteum however is very thin, averaging only 10-40 µm in thickness, consisting of an indistinct connective tissue layer and a few layers of cells. It is thought to have similar functions to the periosteum, contributing to bone repair and reconstruction, as it houses osteoprogenitor cells such as MSCs and preosteoblasts. [67]

1.4.2 Alveolar Bone

Maxillary and mandibular bone is composed of two major types: the external cortical bone and the internal cancellous bone. The outer cortical bone is found on the buccal, lingual, and crestal surfaces of alveolar ridges. This cortical bone is very dense, compact, and has very few blood vessels, especially in the mandibular jaw. Within the cortical bone is the inner cancellous bone. This trabecular, or cancellous, bone runs inside the compact bone and is generally surrounded by a marrow that is highly cellular and unlike the cortical bone, has a rich blood supply. [64] Osseous tissues of cortical bone and cancellous bone are biochemically identical, but structurally distinct.

One way the alveolar bone is classified is based on these structural differences. For instance, in 1988, Misch *et al.* proposed four major bone density groups based on macroscopic cortical and trabecular characteristics: *D1* bone was described as dense cortical bone, typically found in the anterior mandible. *D2* bone was described as porous cortical and coarse trabecular bone, often found in the anterior and posterior mandible and anterior maxilla. *D3* bone types had a thinner (porous) cortical layer with fine trabecular regions. This bone is anatomically found in the anterior maxilla and posterior maxilla and the posterior mandible. Lastly, *D4* bone was described as fine trabecular bone, typically located in the posterior maxilla. [68] A very soft bone, with incomplete mineralization and large intratrabecular spaces has been referred to as *D5* bone. This bone type is often found in the immature bone of a developing bone graft site.

The osseous tissue consists of an organic phase of mainly collagen fibers, which function to give strength, flexibility, and resistance to torsional force, and an inorganic phase of mainly hydroxyapatite crystals, which function to give the bone resistance to compression [69] Inner bone marrow tissue is considered a "blood organ". It possesses important stem cells that are important for bone regeneration. It is a niche for hematopoietic stem cells, which can regenerate whole blood systems from as little as one cell.

1.4.3 Cellular Biology

In bone, there is a balance between bone-formation and bone resorption that is modified throughout life. Regulation is through various bone forming cells (MSCs, pre-osteoblasts, mature osteoblasts, bone-lining cells, and osteocytes) and bone resorbing cells (osteoclasts, macrophages, and multinucleated giant cells, all derived from bone marrow hematopoietic stem cells). [69] More recently, researchers discovered another cell type found in bone tissue, the osteomac, which is thought to be important in bone remodeling and homeostasis. [70]

Osteoblasts and osteoclasts are the two cells that are known to be responsible for both growth, development, deposition, and remodeling of bone. Osteoclasts are responsible for the resorption of bone. They are multinucleated cells that derive from hematopoietic progenitors in the bone marrow which also give rise to monocytes in

peripheral blood. [71] Osteoblasts, on the other hand, are known to lay down new bone and are derived from local osteoprogenitor cells. These osteoprogenitor cells, or preosteoblasts, originate from mesenchymal stem cells within the bone marrow. Remodeling of both cortical and cancellous bone involves complex interactions between osteocytes and these two cell types.

A subpopulation of osteoblasts become embedded by mineralized bone and become a different cell type, osteocytes, which form a network of membrane processes that extend throughout mineralized bone. Osteocytes also play a role in bone homeostasis as they are a major source of molecules that regulate the activity of osteoblasts and osteoclasts, such as RANKL and sclerostin. It is believed that they respond to mechanical load, initiate, and direct the remodeling process that repairs damaged bone. [72] Apoptosis of osteocytes is one of most accepted signaling events for targeted bone remodeling, a process whose goal is to renew and maintain bone throughout life. [64] The concept of osteocyte apoptosis inducing bone remodeling was first introduced in the 1960s by Dr. Harold Frost. While studying the regional acceleratory phenomenon (RAP), he suggested that *microdamage* is needed to for the bone to be actively remodeled in order to adapt to a changing mechanical environment.

The osteocyte normally secretes transforming growth factor β (TGF-β), which inhibits osteoclastogenesis. When osteocyte apoptosis occurs in response to mechanical trauma, such as piezoelectric stimulus for example, TGF- β levels are lowered, which

removes these inhibitory signals and allows osteoclast formation, one of the key initiators

of bone remodeling. [73] The osteocyte response to various surgical stimuli and their

connections to the bone matrix and the bone remodeling process are believed to be key

drivers in bone and bone graft healing.

1.4.4 Bone Healing

A fundamental knowledge of bone healing is necessary to understand the

complexities of various bone grafting techniques. After initial stimulus/injury bone will

heal either by direct intramembranous or indirect fracture healing, which consists of both

intramembranous and endochondral bone formation. Frost *et al.* divided the bone

response to injury/fracture stimulation into five stages. [54]

    A. Bone intervention (e.g., fracture, injury)

    B. Granulation tissue (temporary healing involving soft tissues)

    C. Callus formation

    D. Lamellar bone formation

    E. Recontouring/bone modeling

Our body's biological response to any tissue injury begins with an inflammatory

response. The sites of stimulus send downstream signals which recruit various immune

and host defense cells. [73] During this inflammatory response, or state of temporary

healing, fibroblasts and lipoblasts are involved in the healing process by synthesizing and secreting various intracellular materials such as the collagen networks, which form the preliminary complexes unto which the healing tissues mature. Neovascularization brings blood vessels to the site and soft granulation tissue is formed. This granulation tissue gets resorbed by macrophages and replaced by a new colony of cells which include chondroblasts and osteoblasts. These cells mineralize the extracellular organic matrix of cartilage and woven bone to create a callus. [74] The osteocyte response and the callus itself prompts the basic multicellular unit (BMU) to increase osteoclastic activity (activation stage) and subsequently osteoblastic activity. The presence of mature osteoclasts leads to a retraction of the bone lining cells from the bone surface, allowing the osteoclasts to bind. Howship's lacunae are formed as a result of the osteoclastic bone resorption. Collagen fragments are removed by specialized cells (reversal stage) and osteoblasts deposit type 1 collagen osteoid matrix, which serves as a scaffold for hydroxyapatite crystal deposition (formation phase). Although, most osteoblasts will die off, however a small proportion of them will remain embedded in the newly formed bone as new osteocytes (or will remain on the surface as bone lining cells). When the formation phase is finished, the bone enters a quiescent phase, where remineralization will continue. [75]

1.5 Animal Models in Translational Research

Studies of bone modeling/remodeling and bone graft healing require experimental subjects with human-like bone and therefore rats (*Rattus norvegicus domestica*) were

23

chosen as their bones are sufficiently similar to those of human beings. We chose the

Sprague-Dawley rat, an outbred strain used extensively in medical research and a tibial

model of bone healing was selected based on its size relative to our available surgical

armamentarium and materials and its location allowing for easy surgical access.

1.6 Neural Networks & Deep Learning

Artificial intelligence (AI) refers to "the ability of a digital computer or computer-

controlled robot to perform tasks commonly associated with intelligent beings". [76] AI

has undergone a massive evolution in bridging the gaps between the capabilities of

humans and machines. Researchers and doctors alike, work on numerous aspects of the

field to make remarkable things happen, such as image and video recognition, image

analysis and classification, recommendation systems, natural language processing, etc.

And AI research within medicine and dentistry is growing *rapidly*. In 2016, healthcare AI

projects attracted more investment than AI projects within any other sector of the global

economy, [77] and these numbers are expected to continue to grow especially after the

COVID-19 pandemic.

Machine learning is a subset of artificial intelligence where a computer can learn

and improve its assigned task utilizing internal statistical techniques (vs. human

programming). [78] *Deep learning* is a subset of machine learning in which artificial

neural networks can learn from data and can extract various features available/present

within the data set(s). Artificial neural networks are designed to recognize patterns in

data. They are modelled after the biological neural networks that are found in animal brains. [79] Convolutional neural networks (CNN) are specialized for image recognition tasks. These CNNs can "learn" to perform a variety of tasks by being shown human-engineered examples, instead of being programmed to do such tasks or relying only on statistical methodology. Deep CNNs have demonstrated excellent image classification capabilities, impressive problem-solving abilities, and are believed to hold a large place in future dental/medical research. [80]

1.6.1 From 2D to 3D μCT Analysis

Three-dimensional micro-computed tomography (μCT) is a powerful tool for visualizing and analyzing 3D structures. μCT data typically contains approximately 600 to 1,000 slices of data and this data can be manipulated and used for virtual sectioning and measuring through image stacks. Working with bone/hard tissue samples, sectioning and staining them for histology is inarguably a very time-consuming and technique-sensitive task. With μCT scans, one can easily view hundreds of different slices of a sample virtually – in a matter of hours, in a way visualizing more than what you may see after histological sectioning. Although histological analysis is the gold standard for biological research, it is indeed an arduous process and μCT data is able to predictably yield quantifiable data to study and analyze, especially with calcified hard tissue (bone) samples. For this study, given the project's goals and time constraints, micro-computed

tomographies were used for data collection and analysis after various hard tissue augmentation techniques were tested in a rat tibia model.

The selection of resolution for μCT imaging is a critical parameter that, if not chosen adequately, would have high impact on the data collection/segmentation results. Since we are studying healing in rat bones, it is important to choose a pixel/voxel size that can adequately capture the rat's trabecular architecture. For most human samples, a resolution of 20-60 μm is most often recommended. For mice, 5-10 μm is typically used, and for rat samples 10-35 μm is typically recommended for easily analyzable cortical and trabecular bony architectures.[81] Hence, for this study, a scanner resolution of 10.043 μm (pixel size) was used to ensure an appropriate amount of detail in our scans. Properly segmented μCT data of a bone sample can provide us various 2D and 3D data (based on traditional static bone histomorphometry) such as isolated areas/volumes of interest, different three-dimensional structural parameters, bone thickness, bone porosity, and various bone areas/volumes for both cortical and woven bone.

In order to study the *quantitative* differences in our samples, the total volume of newly formed bone over the recipient site(s) was isolated from our μCT data and a normalized ratio of new bone formation to total bone volume (%) was used for comparison. This selection was based on architectural differences of the various bone grafts tested (*Xenograft, Alloplast, Collagen*) and variations in the available regions of interests (ROI)* for each group studied (*Bur, Piezo, Onlay*). This metric (%) has been

reported as a valid system of measurement when assessing new bone formation in similar

µCT experimental models. [82] [83] [84] To analyze the *qualitative* differences in our

samples, the total porosity (%) of the newly formed bone was measured for each sample

(per SCP) and compared with the total porosity of the native cortical bone of a *Control*

group. One method to collect such data would be to manually segment all slices of data,

however this would be too tedious and time consuming given that each scan has

approximately 1,000 slices of data. This would require ~40,000 manual segmentations.

Since µCT scans of bone samples have varying ranges of radio-opacities, various

thresholding techniques (such as Otsu's method) or Hounsfield units could be used for

segmentation, however due to the complexity and multi-class nature of our samples, we

need more than feature-detection based on radiographic intensity. [85] [86] [87] A blend

of human intelligence with the speed of a computer was required for this task and

machine learning was the answer.

NOTE: This method will be further explained in CHAPTER 2.

We designed a powerful convolutional neural network (CNN) algorithm that was

created and adapted from other work done with our research group (Di Battista, 2020) to

segment the features of interest accurately and effectively from each of our samples to be

analyzed. The segmented outputs from our algorithm are an overlay on top of the raw

µCT data and do not affect the raw data in any way.

1.6.2 The Convolutional Network (CNN)

The goal for neural networks is to enable machines to view and perceive things as humans do, and use the knowledge for a multitude of tasks such as image recognition, image analysis, and image classification in medical research. The advancements in this scope combined with deep learning has been developed and refined with time, primarily with one particularly successful algorithm – the convolutional neural network (CNN). As mentioned before, the architecture of a CNN is analogous to that of the connectivity pattern of the neurons in the visual cortex. Individual neurons respond to stimuli only in a restricted portion of the visual field (the receptive field). And a compilation of these portions overlap to cover the entire visual area.

A simplified outline of the convolutional neural network structure is illustrated in *Figure 1*. The CNN is a deep learning algorithm which can take an input volume, assign importance (learnable weights and biases) to various aspects/areas in the volume and differentiate one from another. The pre-processing required with a CNN is much lower as compared to other classification algorithms. [88] Initial stages of developing a CNN involve hand-engineered training data, but with enough training CNNs can effectively learn these characteristics and output features of interest for statistical analysis.

A "well-trained" CNN can effectively capture the spatial and temporal dependencies in a volume through the application of relevant filters. The architecture performs a better fit to the volume dataset(s) due to the reduction in the number of

parameters involved and reusability of weights. In other words, the network can be

trained to understand the complexity and patterns of the image.
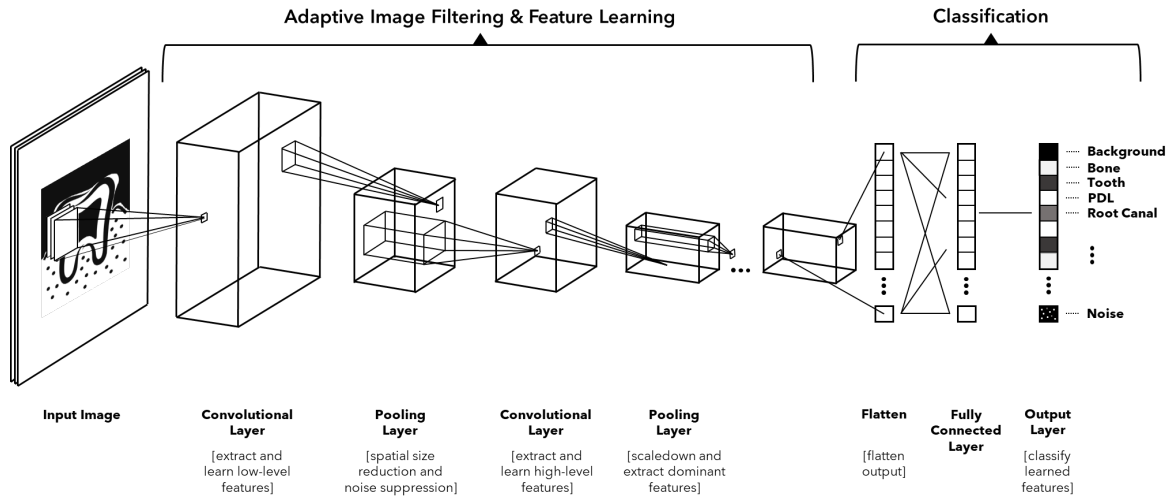
Figure 1. Convolutional neural network structure.

A CNN will extract low level features (major edges, color, gradient orientation,

etc.) from an input dataset into a form which is easier to process, without the loss of

details critical to getting an accurate segmentation. By adding pooling layers, the spatial

size of the convolved feature is reduced, and the computational power required to process

the data is decreased significantly through dimensionality reduction. The pooling layers

will also extract dominant features from your samples (rotational and positional

variations) and further convolutional layers will then extract the higher-level features

(minor edges, etc.) as further pooling layers will reduce noise. [89] This training

continues until the network has a completed understanding of the volumes/areas in the

dataset(s). For more complex volumes, the number of convolutional layers and pooling layers needs to be increased as does the computational power. [90]

After completing a series of epochs in the above process, the final output is flattened and fed into a regular neural network for classification and multi-level feature extraction purposes. Our multi-class segmentation (Original Cortical Bone, New Bone Formation, Background, Bone Graft Material) algorithm utilized a U-net training architecture [85] and each sample had value accuracy rates of over 99.9% when self-verifying after training. After whole scans were segmented, the results were optimized by hand with another trained researcher to ensure that no features were mis-labelled.

RESEARCH PROJECT

Hypothesis

We hypothesized that selective cortical penetrations created using the piezoelectric knife may lead to enhanced cellular activation during bone regeneration when compared with conventional bur or subperiosteal onlay grafting methods.

Aim

The aim of this project was to evaluate and compare both the quantity and quality of new bone formation when using a piezoelectric knife (versus the conventional bur and onlay grafting techniques) to prepare the recipient site in bone regeneration surgery. This was done by using X-ray microscopy and deep learning analysis.

CHAPTER 2

MATERIALS AND METHODS

2.1 Outline

The study was approved by the Boston University Medical Center Institutional Animal Care and Use Committee (BUMC IACUC) for all animal procedures in this study (protocol AN-15682). The animals were purchased from Charles River Laboratories International and acclimatized in the Laboratory Animal Science Facility for at least 2 days (48 hours) prior to performing the surgeries. A total of 20 Sprague-Dawley male rats were used. The animals were all 9-to-10-week-old male Sprague-Dawley rats, weighing around 300-350g. The pre- and post-operative weights of the rats, their levels of pain/distress, and hematological data at the time of sacrifice were closely monitored at Boston University's Animal Science Center in order to assess the peri-experimental systemic health of the rats. The experimental groups were divided as follows: A piezoelectric knife (BS1 insert) of the Piezotome 2 (Satelec®, Acteon group, Merignac, France) was used to create four selective cortical penetrations (trans-cortical) on the tibia and the recipient sites were grafted using either a *Xenograft* (Bio-Oss Collagen, Geistlich Biomaterials), an *Alloplast* (OsteoGen, Impladent Ltd), or a *Collagen* matrix (Mucograft, Geistlich Biomaterials) (*PIEZO group*). A conventional surgical carbide bur (#1/2) was used to create four selective cortical penetrations (trans-cortical) on the tibia and the recipient sites were grafted using either a *Xenograft*, an *Alloplast*, or a *Collagen* matrix (*BUR group*). The defects created using a surgical carbide bur were done using a template to ensure that they were similar in size and shape to those created by the BS1

Piezotome insert (Figure 14). A full-thickness envelope flap was created on the tibia with no bone intervention and the recipient sites were grafted using either a *Xenograft*, an *Alloplast*, or a *Collagen* matrix (*ONLAY group*). For the *Xenograft* study groups, special attention was directed to the SCPs on the right tibias and the onlay grafts on the left tibias. For the *Alloplast* and *Collagen* study groups, the surgical techniques were mixed on left/right sides. The rats in the experimental groups were euthanized with 20% CO_2 asphyxia at 28 days post-operatively. Tissue and serum responses were assessed at 28 days. Three 12-week-old male Sprague-Dawley rats with untouched tibias were euthanized and served as controls (*Control* group).

2.2 Grafting Material Preparations

The three grafting materials were prepared under sterile conditions.

2.2.1 Xenograft

For the *Xenograft* groups (Bio-Oss Collagen, Geistlich Biomaterials), a 100 mg preformed block was used. (Figure 2) The block was held in place using sterile cotton pliers and a sterile stainless-steel blade (#15, Bard Parker) was used to create the individual xenograft blocks. (Figure 3) A sterile periodontal probe was used as a guide to create individual xenograft blocks 6 mm in length, 3 mm in height, and 3 mm in width. (Figure 4). The grafts were hydrated with sterile saline prior to surgical placement, per the manufacturer's recommendations.

Figure 2. Xenograft group.

This figure shows the dehydrated 100 mg preformed xenograft block, prior to cutting.

Figure 3. Xenograft preparation.

This figure illustrates how the xenograft block grafts were prepared using sterile cotton pliers, surgical 15 blade, and periodontal probe.
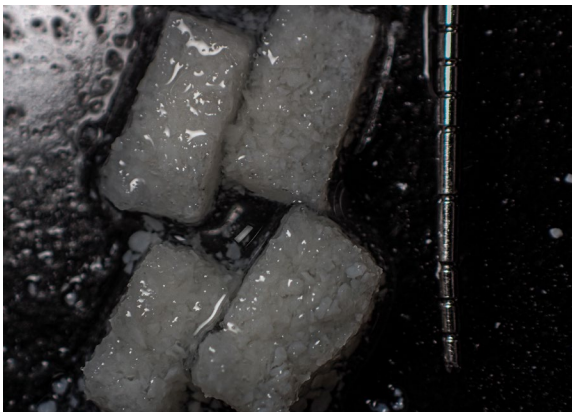
Figure 4. Xenograft dimensions.

This figure shows the final dimensions of the xenograft block grafts hydrated in sterile saline. (~ 6 x 3 x 3, mm)

2.2.2 Alloplast

For the *Alloplast* group (OsteoGen, Impladent Ltd), a 20 mm x 40 mm x 3 mm strip was used. (Figure 5) A 6mm sterile, disposable biopsy punch (Integra Miltex, Fisher Scientific) was used to create equally sized alloplast discs. (Figure 5) The discs were 6 mm in diameter and 3 mm in thickness. (Figure 6) The grafts were not hydrated with sterile saline prior to surgical placement, according to the manufacturer's recommendations.

2.2.3 Collagen Matrix

For the *Collagen* matrix group (Mucograft, Geistlich Biomaterials), a 30 mm x 40 mm x 3 mm strip was used. (Figure 7) A 6 mm sterile, disposable biopsy punch (Integra Miltex, Fisher Scientific) was used to create equally sized collagen matrix discs. (Figure 8) These discs were 6 mm in diameter and 3 mm in thickness (Figure 9), as well. The grafts were not hydrated with sterile saline prior to surgical placement, according to the manufacturer's recommendations.
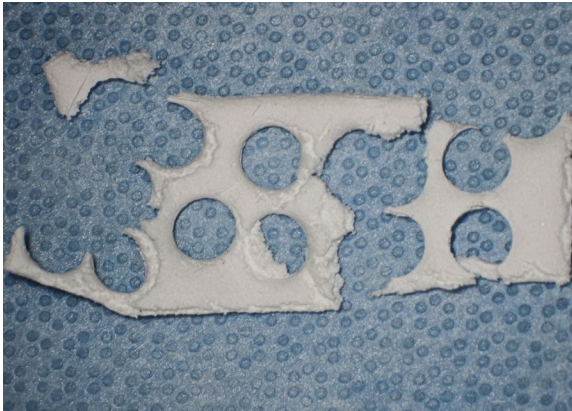
Figure 5. Alloplast group.

This figure shows the alloplast bone strip after the individual alloplast discs were harvested.

Figure 6. Alloplast preparation.

This figure illustrates how the alloplast discs were prepared using a 6 mm sterile biopsy punch.
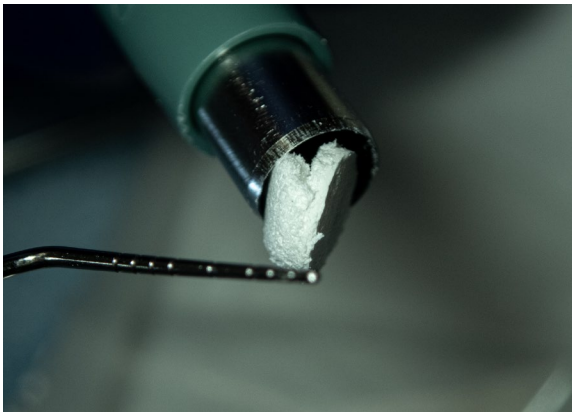
Figure 7. Alloplast dimensions.

This figure shows the final dimensions of the alloplast discs prior to surgical placement. (6 x 3, mm)
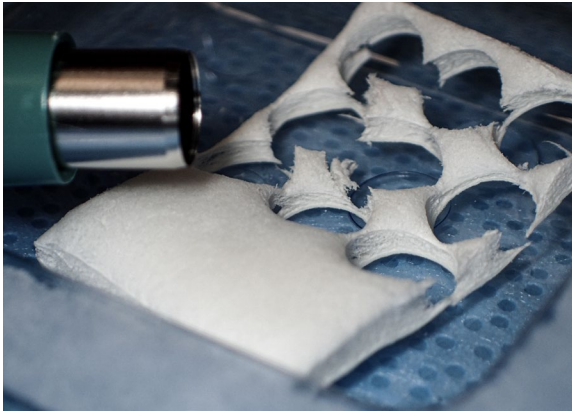
Figure 8. Collagen matrix group.

This figure shows the collagen matrix after the individual alloplast discs were harvested.

Figure 9. Collagen matrix preparation.

This figure illustrates how the collagen matrix discs were prepared using a 6 mm sterile biopsy punch.

Figure 10. Collagen matrix dimensions.

This figure shows the final dimensions of the collagen matrix pucks prior to surgical placement. (6 x 3, mm)

2.3 Surgical Procedure

The animals were fed rat chow and water ad libitum and weighed daily. They were purchased from the vendor and given at least 48 hours to acclimate in the housing area of the Boston University Animal Science Center (ASC) prior to experimentation. They were housed two to a cage. At the time of surgery, the rats were sedated and anesthetized with intraperitoneally-administered ketamine (75-95 mg/kg) and Xylazine (5mg/kg) in one bolus injection. Tail-pinch test was performed to confirm depth of anesthesia prior to procedure. 0.3 mg/kg of subcutaneously-administered sustained-release buprenorphine was given post-operatively for extended-release pain control.

Surgical site preparation began with shaving the mesial surfaces of each rat's legs. An electric clipper was used until adquequate skin exposure was achieved. The skin was sanitized with an isopropyl alcohol solution (70%). The leg was then extended and held in place while an incision was made using a sterile, stainless steel blade (#15, Bard-Parker). (Figure 11) The recipient site was accessed through this full-thickness incision (Figure 12) and was created by raising a full-thickness, "pouch"-like envelope flap. While reflecting the periosteum, special care was taken to avoid damage to the *Tibialis Anterior* muscle. If no selective cortical penetrations are planned, the grafting material would be placed under the flap at this time (*ONLAY group*). (Figure 13)
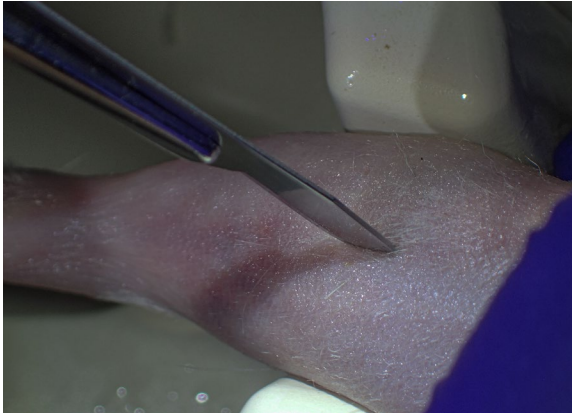
Figure 11. Surgical site preparation.

Full thickness incision is carefully carried out in contact with the shaft of the tibia.
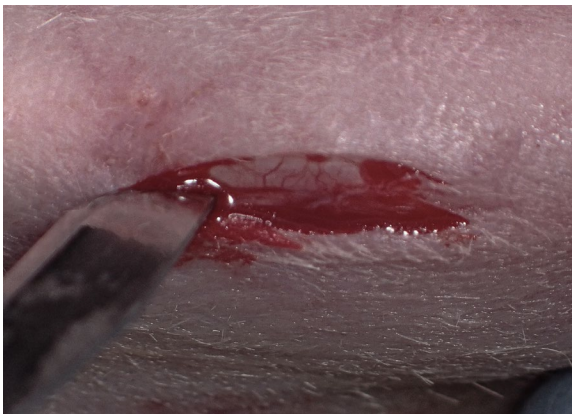
Figure 12. Incision design.

Incision is made with a 15C sterile stainless-steel blade.

Figure 13. Full-thickness envelope flap.

Full thickness mucoperiosteal envelope flap is raised using microsurgical instruments. At this point, if no selective cortical penetrations are planned, the grafting material is placed. (*ONLAY* group)

39

If selective cortical penetrations are planned with a surgical carbide bur (#1/2) (*BUR group*), a custom-made surgical stent was used. This stent was designed with channels of similar size and shape to those created by the BS1 Piezotome insert. (Figure 14) The template is held firmly in place along the shaft of the tibia. (Figure 15) Four [trans-cortical] selective cortical penetrations were created through the channels of the surgical template using an Osseocision dental motor system (Biomet 3i) with a surgical stainless steel carbide bur (#1/2). (Figure 16) The handpiece motor was run at 800 RPM speed with a torque of 20:1 under copious irrigation with sterile saline. Penetration of through the cortical layer of bone was confirmed by visual observation of bleeding from the surgically-created bony defects.
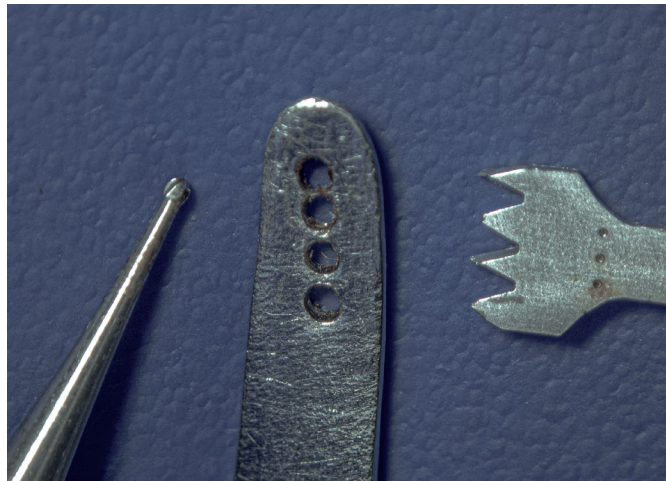
Figure 14. Armamentarium.

Surgical carbide bur (#1/2) (BUR group), custom-made surgical template, piezoelectric knife (BS1 insert) (PIEZO group). If selective cortical penetrations are planned, the carbide bur is used with a surgical template designed to create equally-spaced SCP's.
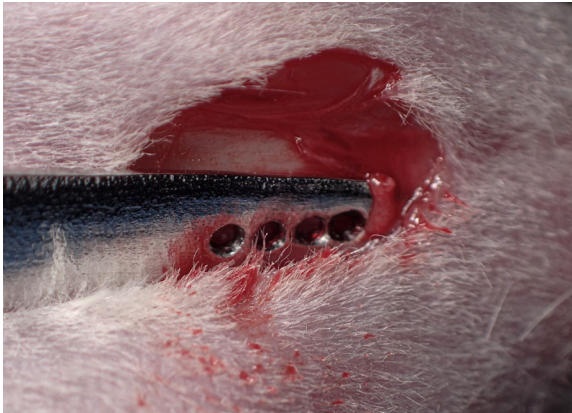
Figure 15. Surgical template placement.

Custom-made surgical template is firmly held in place along the bone surface inside the full-thickness envelope flap.
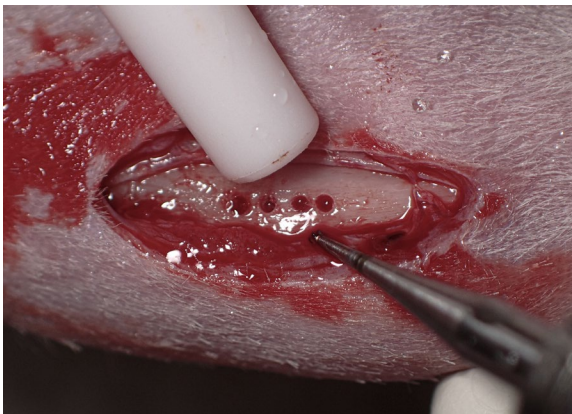
Figure 16. Four selective cortical penetrations created with a surgical carbide bur.

Four SCP's are created with a bur (#1/2) using the surgical template with sterile saline irrigation. The carbide is run at a speed of 800 RPM. Note the bleeding from the marrow space confirming trans-cortical penetration.
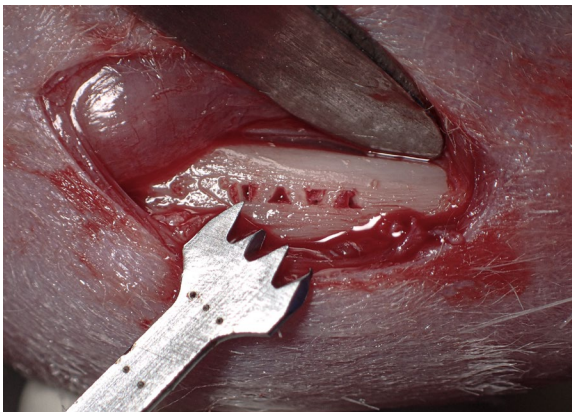
Figure 17. Four selective cortical penetrations created with a piezoelectric knife.

Four trans-cortical SCP's are created using the piezoelectric knife (BS-1 insert).

If selective cortical penetrations are planned with a piezoelectric knife (BS1 insert) (*PIEZO group*), four selective cortical penetrations are made using a Piezotome II unit (Acteon, Satalec). The settings used were modulation of 30 Hz and an irrigation setting of 60 mL/min sterile saline. The four teeth of the piezoelectric knife are inserted until bleeding is confirmed (approximately 1 mm transcortical). Special attention was made to not insert the BS1 insert past the base of the four cutting edges, in order to create four separative selective cortical penetrations. (Figure 17) The grafting materials were then placed under the full-thickness envelope flap using microsurgical instruments and magnification. In recipient sites where selective cortical penetrations were made, the grafting material was placed directly centered over the four cortical defects. (Figure 18) Using three different grafting materials (xenograft, alloplast, collgen matrix) and three different recipient bed preparation techniques (bur, piezo, onlay), this yields 9 different bone grafting techniques (nine experimental groups).
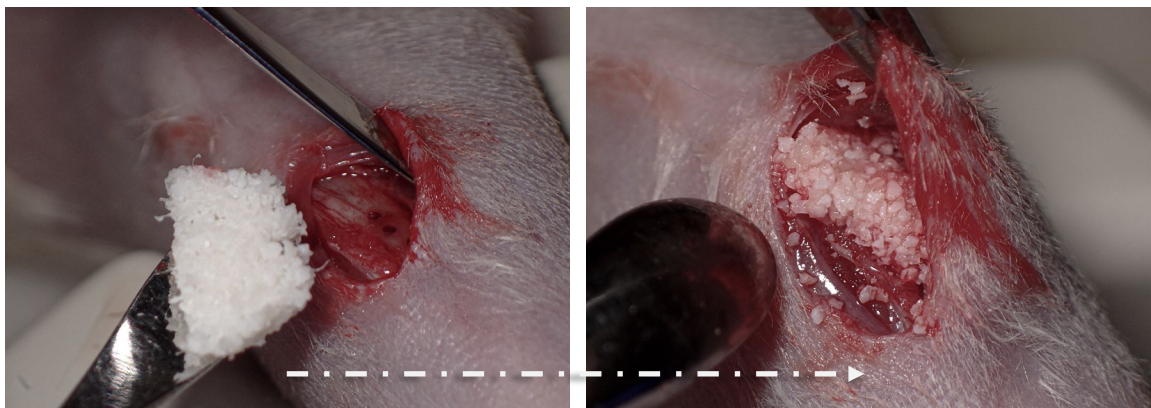
Figure 18. Placement of the grafting material into the recipient site.

This figure illustrates the placement of the xenograft into the recipient site prepared with a surgical carbide bur (*Bur, Xenograft*).

Each of the three grafting materials were fixed over the recipient bed preparation using two mattress sutures: one vertical mattress suture to prevent axial displacement of the graft and one modified horizontal mattress suture to prevent rotational displacement of the graft. (Figure 19) Once the second mattress suture (horizontal) is tightened, the flap edge, including the periosteum, was brought *over* the grafting material. (Figure 20) Finally, a layer of three single interrupted sutures were added to obtain primary closure of the flap edges. The synthetic, resorbable, braided suture strands used were 4-0 polyglycolic acid (PGA) (ACE Surgical) for the two mattress sutures and 5-0 polyglycolic acid (PGA) (ACE Surgical) for the single interrupted sutures.
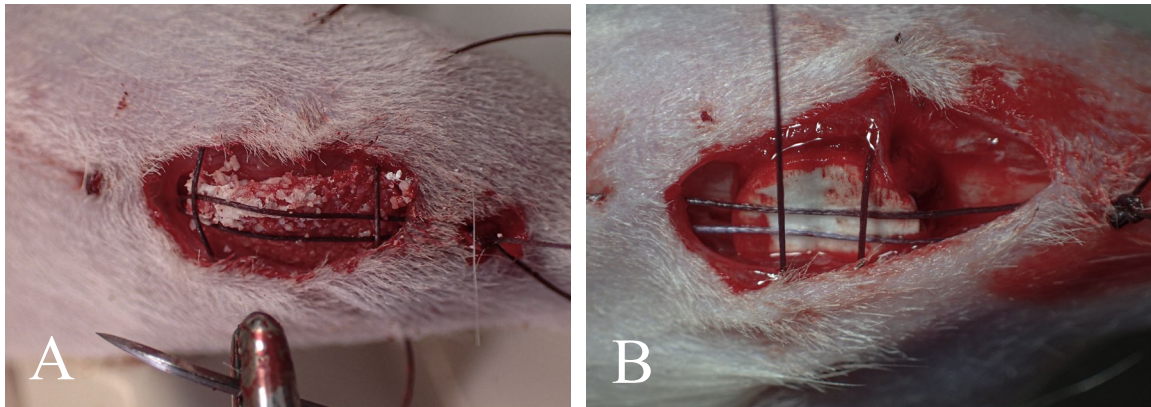
Figure 19. Graft fixation with vertical mattress suturing technique.

This figure illustrates the fixation of the xenograft (A) and the collagen matrix (B) using two mattress suturing techniques. Both the vertical mattress and the horizontal mattress sutures prevent displacement of the graft from the recipient bed.
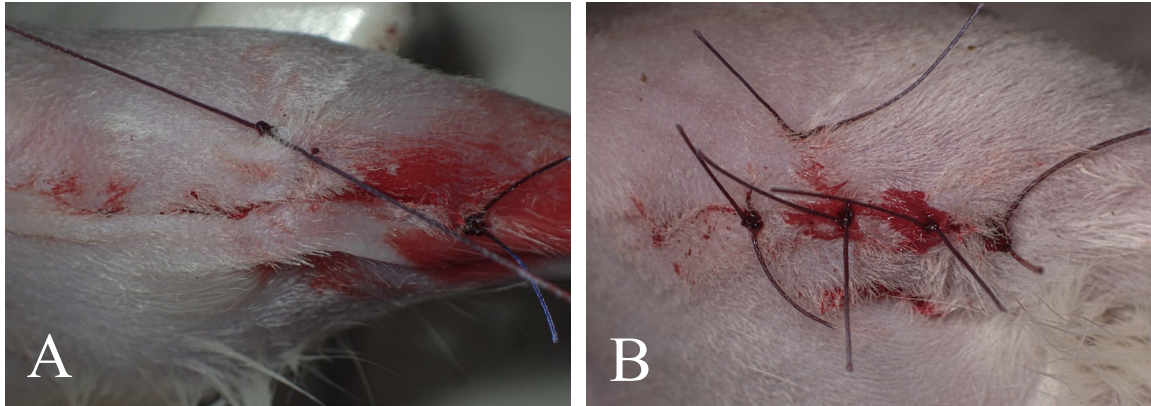
Figure 20. Flap advancement and immediate primary closure.

(A) The horizontal mattress suture brings the full-thickness flap edge over the grafting material and in close approximation with the other border. (B) Three simple interrupted sutures are tied for immediate, low-tension primary closure.

Animals were allowed to fully recover from anesthesia in in their cage over a warm water-filled heating pad with close monitoring. 3 mg/kg of subcutaneously-administered sustained-release Buprenorphine (SRLAB, ZooPharm) was given for 72-hour extended pain control. Once the rats were fully awake, they were placed in their housing room. Their weights and condition were monitored daily for the first 14 days and once weekly until day 28.

At day 28, after euthanization by 20% carbon dioxide asphyxiation, blood was collected from the heart for hematological analysis. The skin was carefully dissected around both legs and the legs (femur, knee, and tibia) were removed at the acetabulofemoral joint. Soft tissues around the tibia were kept intact. The limbs were preserved in 4% paraformaldehyde (PFA) solutions and stored at 4ºC until scanning.

2.4 3D X-ray Microscopy

A high-resolution X-ray microtomography imaging system (Xradia 520 Versa, Zeiss) was used to scan each sample at Boston University's Photonics Center (PHO). This 3D microscope can capture highly accurate non-destructive 3D images utilizing advanced X-ray source technology and high-resolution detectors. This X-ray computed tomography technology has been used in life science research and in advanced material research and development. It is capable of capturing a wide array of contrasts, which allows imaging of hard tissues and less-calcified tissues as well. For this study, a scanning resolution of 10 μm voxel size was used, as previously mentioned.

The Scout-and-Scan Control System workflow (Zeiss) was used to localize the volume of interest along the tibial diaphysis and acquire our tomographies. (Table 1) First, the sample's data folder was set and a new recipe creation was initiated. Second, using the visual light camera, the sample was loaded, roughly positioned on the axis of rotation, and the X-ray source and detector was positioned. (Figure 21) Third, the sample's region of interest (ROI) and field of view (FOV) was located, and the imaging parameter values were set. The region of interest (tibia diaphysis) was found and centered at low magnification. The ROI was then fine-tuned at high magnification. The X-ray source and detector positions were set. The appropriate source filters and voltages were set. The acquisition time was then determined. Fourth, the recipe's 3D scan parameters were set up. Lastly, the recipe was run and the tomographies were acquired.

MICROTOMOGRAPHY IMAGING SETTINGS	
Source Voltage	80.00 *kV*
Source Power	7.00 *W*
Approximate Source Position	-50.00 *mm*
Detector Position	205.00 *mm*
Scan Duration	*~2 hours*
Objective Magnification	0.4 X
Field Mode	Normal
Source Filter	LE1
Pixel Size	10.043 *μm*

Table 1. Scout-and-Scan Control System settings for μ-CT.

This table outlines the scan settings for the Scout-and-Scan Control System (Xradia 520 Versa, Zeiss).

Figure 21. Volume of interest localization using 3D x-ray microscopy.

This figure illustrates the technique used for localizing and scanning the samples. Note the image on the right, which shows how the samples were loaded into the scanner using a custom-made falcon tube base.

2.5 Deep Learning

2.5.1 Training Input

As discussed earlier in the introduction, for our project, we did not have the time nor manpower to segment each slice of every micro-CT scan individually, so we elected to design and use a deep learning algorithm for segmentation and data extraction. Various software packages can be used for this type of CNN design, however we used Dragonfly (ORS Systems) because of its wide range of image analysis capabilities and ease of use. First, we hand segment 8 slices of every scan to feed our algorithm. (Figure 22) These "ground truths" were verified with another experienced investigator. This is the "example" that we give to the computer that we will feed the training model in order to allow for it to "learn" as mentioned previously.

The purpose of this step is to provide our model will a learning set containing the original, unaltered micro-CT scans ("what we are beginning with") and also to provide our segmented target output to show the algorithm "what we want to end up with".

47

Hand-Engineered Segmentation Data (8 Slices) for CNN Feature Detection

Training Input
Multiple samples are fed into the deep learning algorithm.

Target Output
Filtered training data sets are used in the deep learning model.
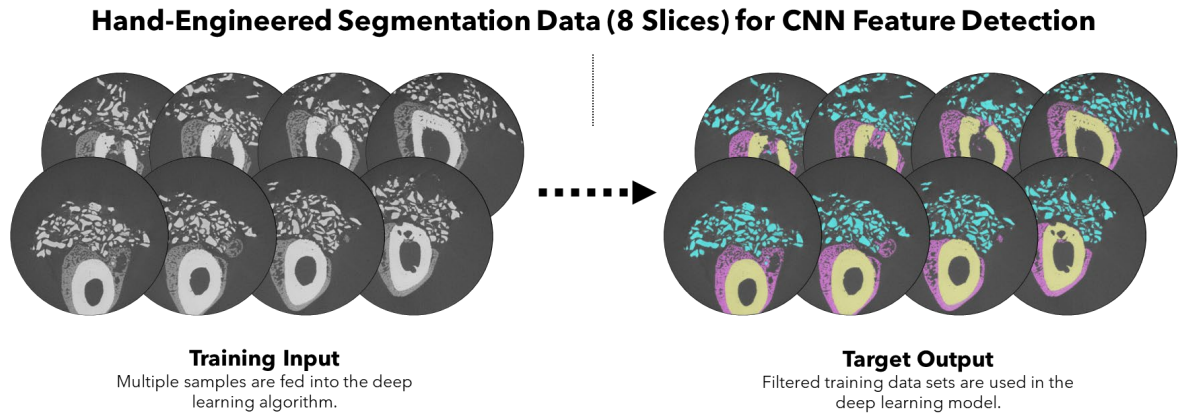
Figure 22. Deep learning input data.

Figure 22 shows a simplified version of the input that is fed into the preliminary convolutional neural network algorithm. Several iterations of the training data are layered for feature detection and deep learning modeling.

2.5.2 Other Modelling Parameters

Training a deep learning algorithm can take weeks if not months depending on the optimization algorithm used and the computational power available. For our project, we elected to use a CNN as discussed earlier and the method for optimization utilized was the AdaDelta algorithm. This unique learning rate method helps minimizes the value of the function loss by dynamically adapting its learning memory overtime with scaled down datasets (a decaying average of all past squared gradients) and therefore has remarkably minimal computational overhead. [91]

Minimizing function loss is analogous to minimizing error in our deep learning model - the more error in our algorithm, the less accurate our segmentation outputs will be. And loss functions are used to calculate how well our deep learning model is

48

modelling given the 8 slices of training data. For our project we have a multi-level

segmentation target output (new bone, original bone, bone graft, and background),

therefore our algorithm's errors can be multi-level. For feature recognition, the problems

we face are mostly binary on each individual feature level. For example, if our deep

learning algorithm tags a particular pixel as new bone, when in reality it is a bone graft

particle, this needs to be recognized as an error based on our training data sets. [92]

Categorical cross-entropy is the loss function model chosen for our multi-label

segmentation because researchers on our team have had accurate segmentation results

with this method.

DEEP LEARNING ALGORITHM MODELING PARAMETERS	
Architecture	U-Net (5-level)
Model Type	Multi-label Segmentation
Class Count	4
Input (Patch) Size	128
Stride to Input Ratio	0.5
Epochs Size	50
Loss Function	categorical_crossentropy
Optimization Algorithm	Adadelta
Memory Ratio	< 1.0
Data Augmentation Used on Input Data	Rotation, Mirroring, Shearing, Scaling
Percentage of Training Data to be Used for Validation	25%

Table 2. CNN algorithm modeling parameters used in Dragonfly's deep learning tool.

This table outlines the modeling parameters for the Deep Learning Tool (Dragonfly, ORS) for reference.

Table 2 outlines the parameters set for the Deep Learning Tool in the 3D visualization and analysis software application. Note that 50 epochs were used in this algorithm simply because our hardware did not have enough processing power for more. All models, however, had value accuracy rates of over 99.0% when self-verifying after training and a maximum value loss of 0.03% after Epoch 50 out of 50. A sample of the resulting output segmentation from our deep learning algorithm is shown in Figure 23. You can appreciate the successful feature detection of the output data with impressive distinctive abilities between original cortical bone, bone graft material, new bone formation, and background.
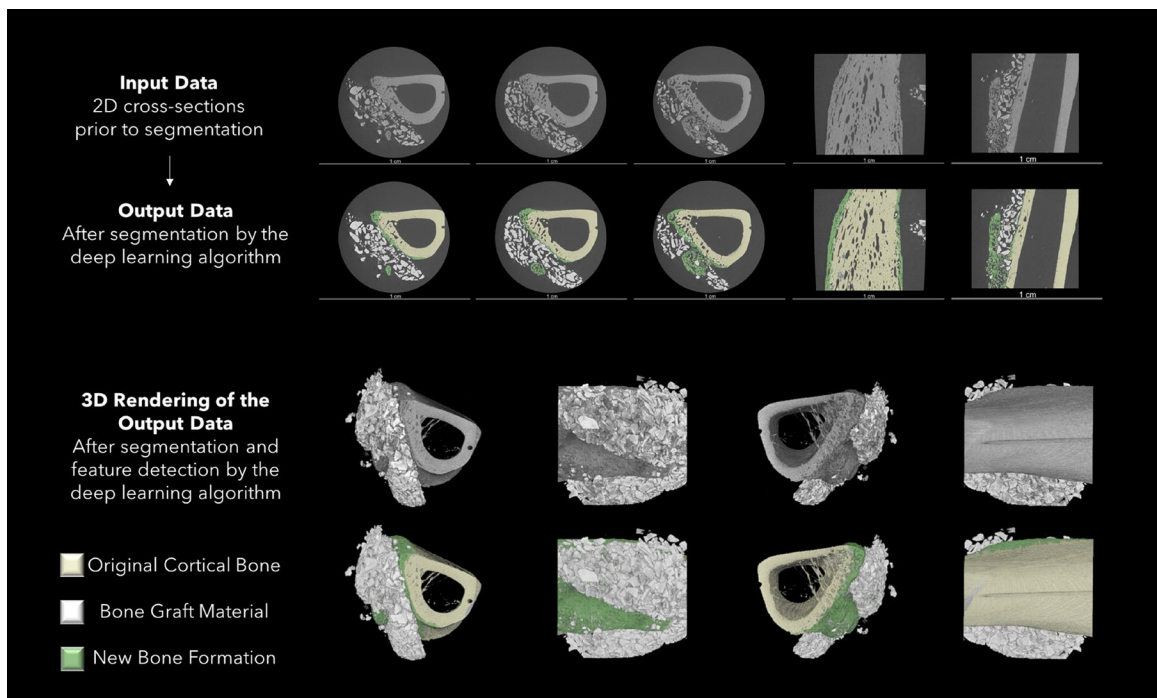
Figure 23. Example output of the deep learning segmentation.

The top two rows show a cross-sectional representation of an original sample (onlay technique with xenograft) that is fed through our deep learning segmentation algorithm. The bottom rows show a three-dimensional rendering of the input-output data.

2.5.3 Data Acquisition

After whole scans were segmented using these algorithms, the resultant segmentations were manually optimized to ensure that no features were obviously mislabeled. This was cross-checked with another blinded, experienced researcher. The output was essentially an overlay on top of the raw data, with no effects on the original data in any way. The models showed successful feature recognition of the original cortical bone with new bone formation around the surgical sites, often with residual bone graft particles encapsulated within the newly formed calcified tissues. The data extracted from the whole scan segmentations, however, included the volume of new reactive bone formation [μm^3], the volume of original tibia cortical bone [μm^3], and the volume of the graft [μm^3]. Since the whole scans were taken at 10 μm resolution and the surgical sites ranged from 3.5 – 6 mm in distance, a region of interest (ROI) needed to be established for each sample in order to extract data from the area where grafting was completed only. Because of the differences in surgical site dimensions and also because 2 of our 20 scans were out of alignment (missed 2 of the 4 SCPs), the ROI could not be standardized across all groups. The ROI was defined based on the following criteria: (1) When SCPs were used, the ROI must be within the beginning of the first defect and the end of the last defect, (2) If identifiable, the graft must be within both ends of the intracortical defects within the range described above (underlying the graft), and (3) When no decortications were used (*Onlay* group), the ROI was defined as the tibial volume above which grafting material was overlaid. Figure 24 shows an illustration of how the ROI was selected for each sample.

51
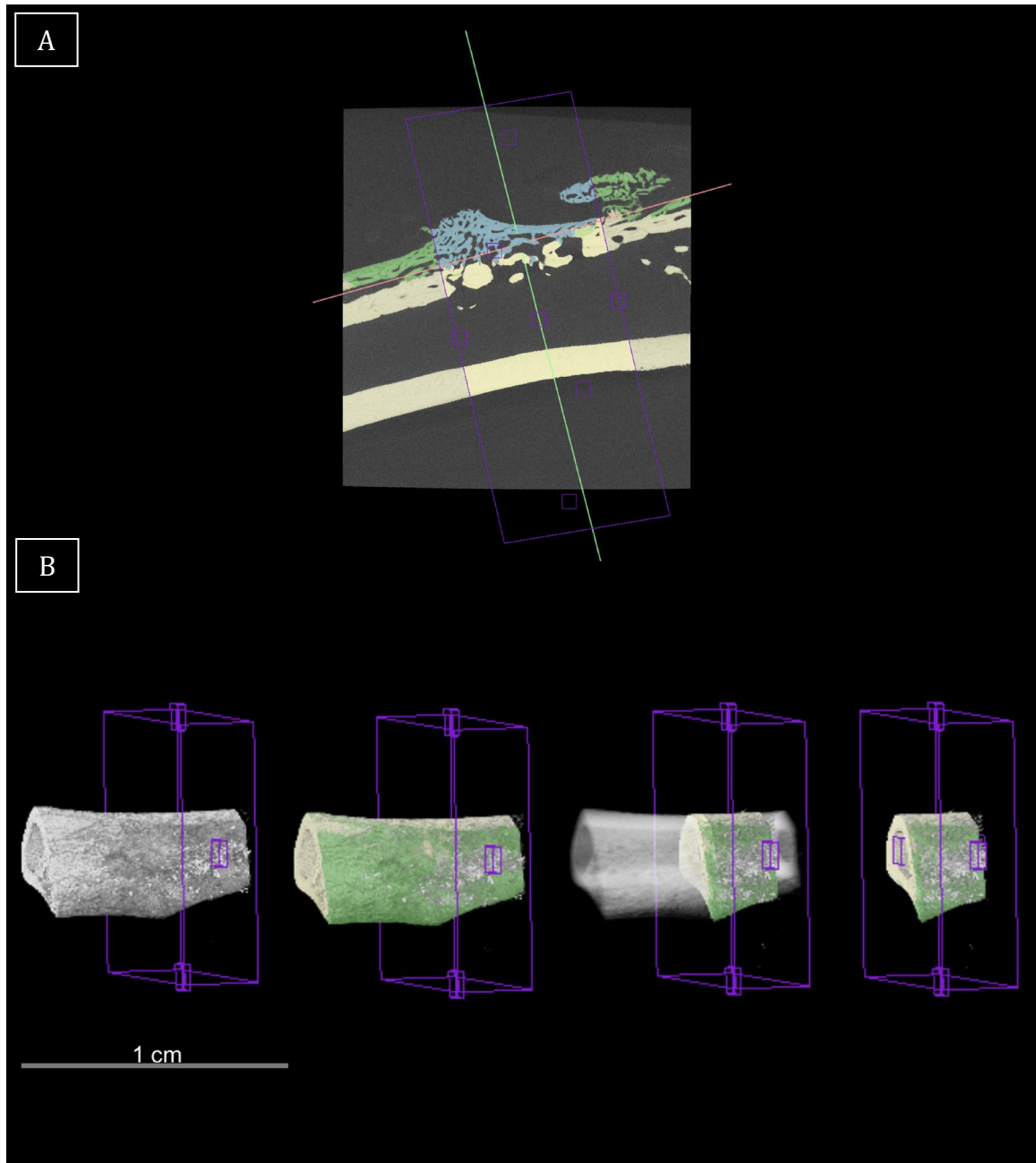
Figure 24. Region of Interest (ROI) Isolation

Figure 24 shows a cross sectional view of a region of interest (in purple) highlighted around the four selective cortical penetrations. Figure B illustrates a three-dimensional view of the ROI defining steps. Note each ROI is selected perpendicular to the long axis of the tibial diaphysis.

Once again, when conducting our quantitative analysis of the newly formed bone for each study group, due to the differences in size and architecture of our volumes of interest (ROIs), the data was normalized for each sample by calculating a ratio of new bone volume to total bone volume. Also, the total porosity of the newly formed bone for each study group plus the 3 control samples was calculated using a technique illustrated in Figure 25. For porosity analysis, a new ROI needed to be created (the area or volume of space occupied by the newly formed bone – including the background/marrow spaces – in blue). The deep learning algorithm was not successful when detecting the new ROI for porosity analysis in whole scan samples. So, after the original multi-level segmentation algorithm was run, one slice per SCP was randomly selected to manually create this new ROI. Then the surface area of newly formed bone was divided by the surface area of the ROI to arrive at a density measurement which was easily converted to total porosity in Excel (Microsoft 2013).

Sample μ-CT Scan
Sample is run through our deep learning algorithm.

Feature Detection Output
New bone formation is extracted from the deep learning model.

New ROI For Porosity Analysis
A new region of interested is selected for density analysis.
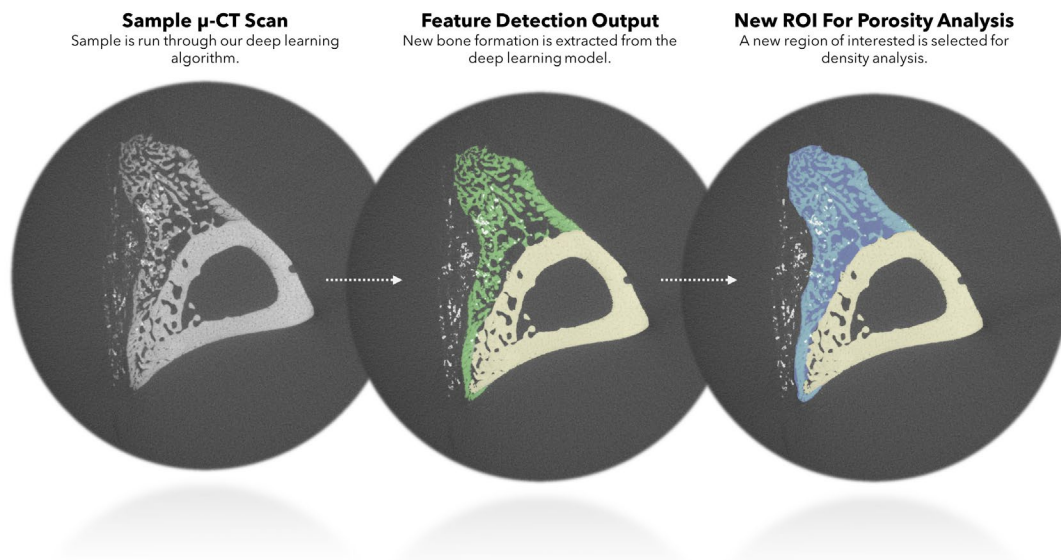
Figure 25. Total Porosity Analysis Example.

2.6 Hematological Analysis

Blood was isolated from each rat immediately following carbon dioxide asphyxiation by cardiac puncture. [93] The blood was transferred to heparin-coated blood collection tubes (VACUETTE, Thomas Scientific). After centrifugation and isolation, the serum was tagged and frozen at -80°C. Each rat's blood was analyzed using a Hemavet 950 FS blood analyzer (Drew Scientific), using the Mascot hematology profile. All samples were analyzed within 24 hours of collection.

2.7 Statistical Analysis

Statistical analysis was completed using the software JMP Pro 15 (SAS Institute Inc, Buckinghamshire). Analysis of variance (ANOVA) was used. For new bone formation measurements and total porosity, the ANOVA test was utilized with a power of 95%. Statistical differences were considered significant at the 5% critical level. If a statistically significant difference was observed between means, Tukey honest significance test (HST) was applied to each pair to investigate which ones differed significantly. Lastly, the Dunnett's test was used to compare total porosities to the control.

The tables with values for each sample's raw μCT data, raw hematological data, and raw weight monitoring data are available in the A*ppendix*.

CHAPTER 3

RESULTS

3.1 3D X-ray Microscopy

3.1.1 Segmentation Overview
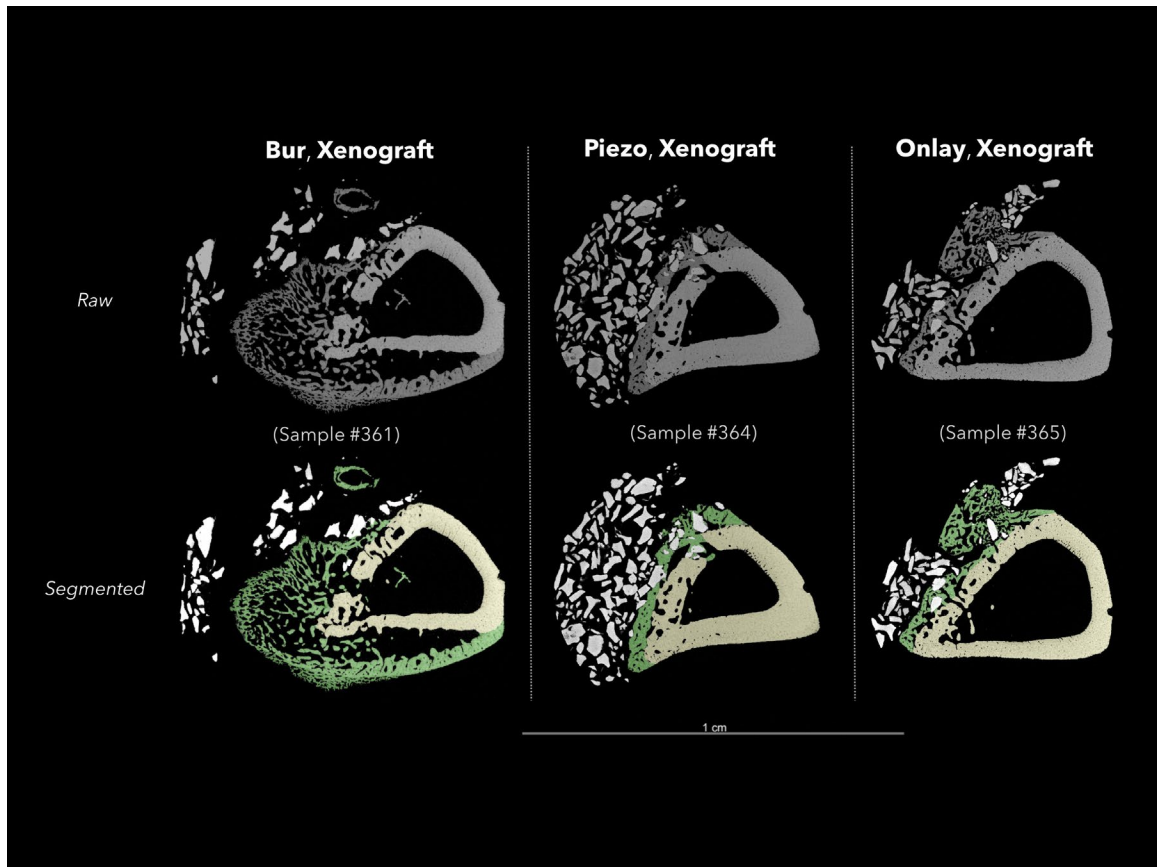
Figure 26. Segmented Xenograft samples.

Figure 26 shows the result of the segmentation for one sample of each X*enograft* group (*Bur, Piezo, Onlay*) on a longitudinal cross-section (slice). The original cortical bone is segmented in yellow, the newly formed calcified tissue in green, and the residual bone graft particles are white.
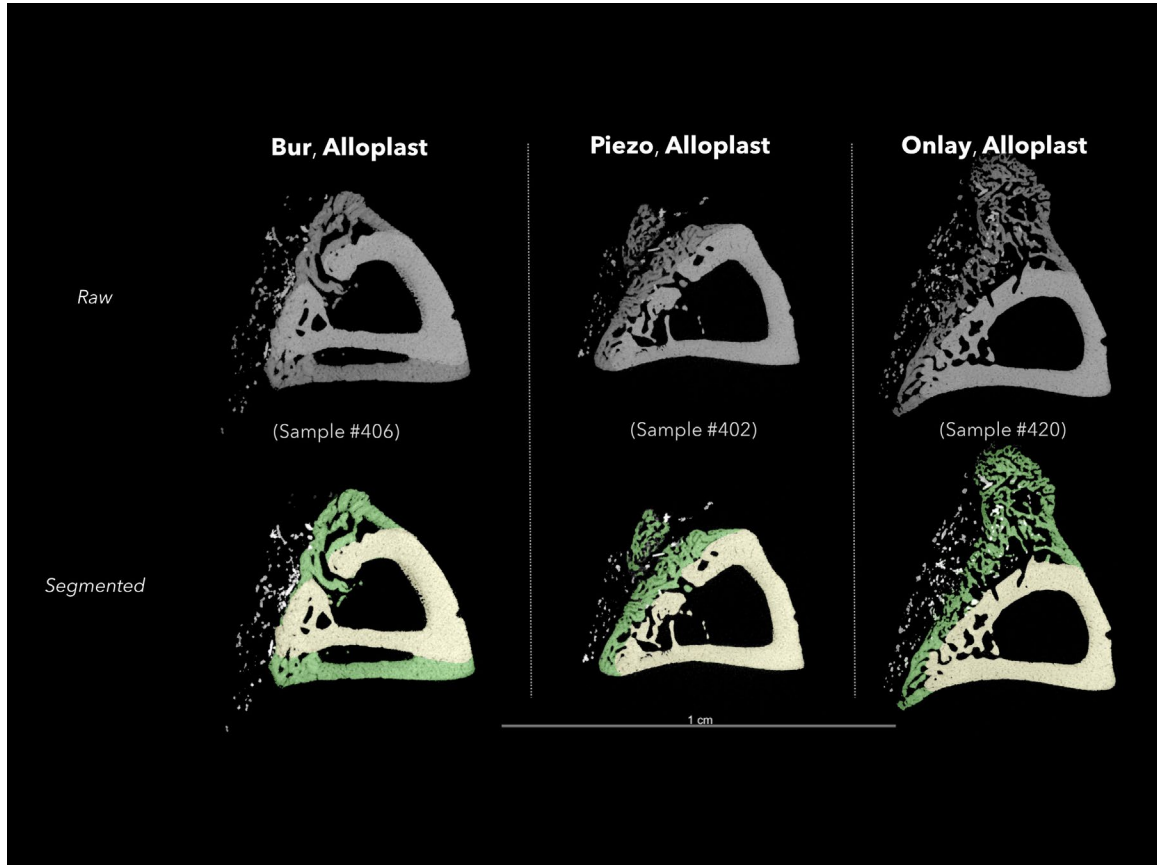
Figure 27. Segmented Alloplast samples.

Figure 27 shows the result of the segmentation for one sample of each *Alloplast* group (*Bur, Piezo, Onlay*) on a longitudinal cross-section (slice). The original cortical bone is segmented in yellow, the newly formed calcified tissue in green, and the residual bone graft particles are white.
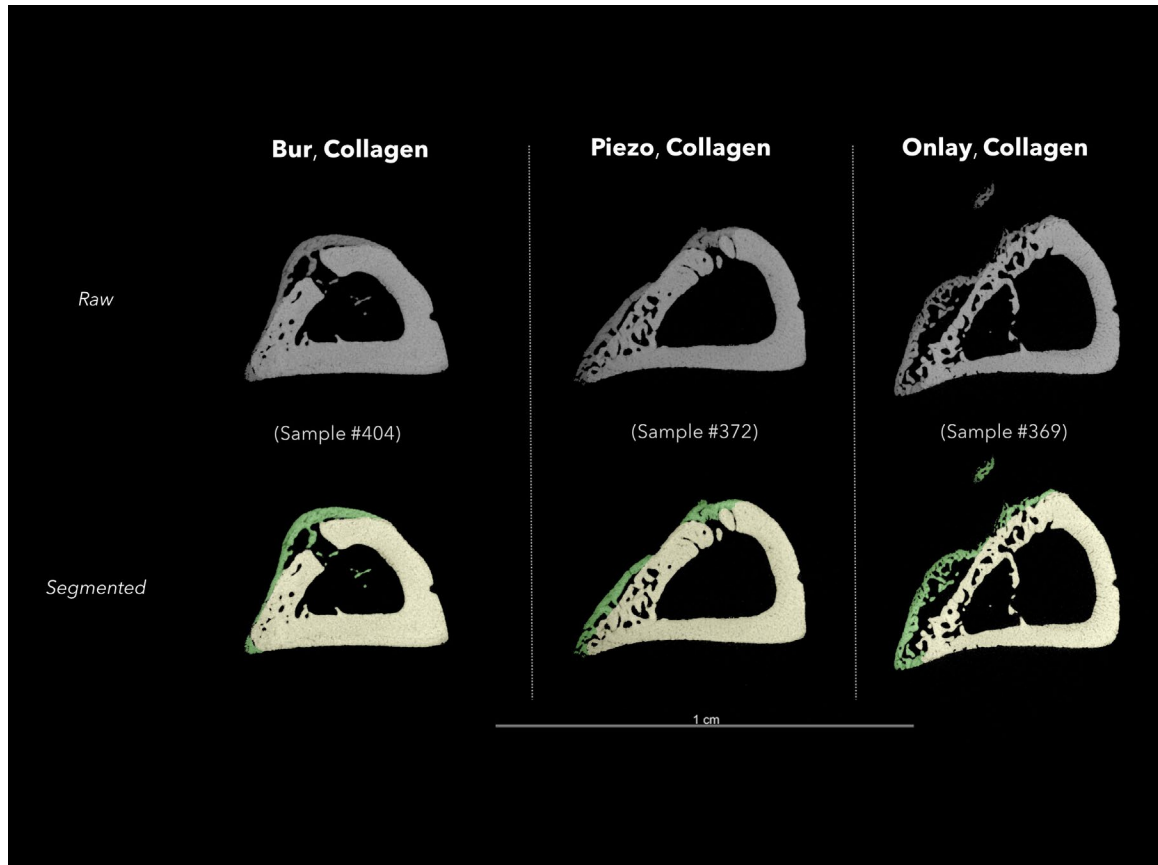
Figure 28. Segmented Collagen Matrix samples.

Figure 28 shows the result of the segmentation for one sample of each *Collagen* matrix group (*Bur, Piezo, Onlay*) on a longitudinal cross-section (slice). The original cortical bone is segmented in yellow, and the newly formed calcified tissue is green.

3.1.2 Volumetric Analysis
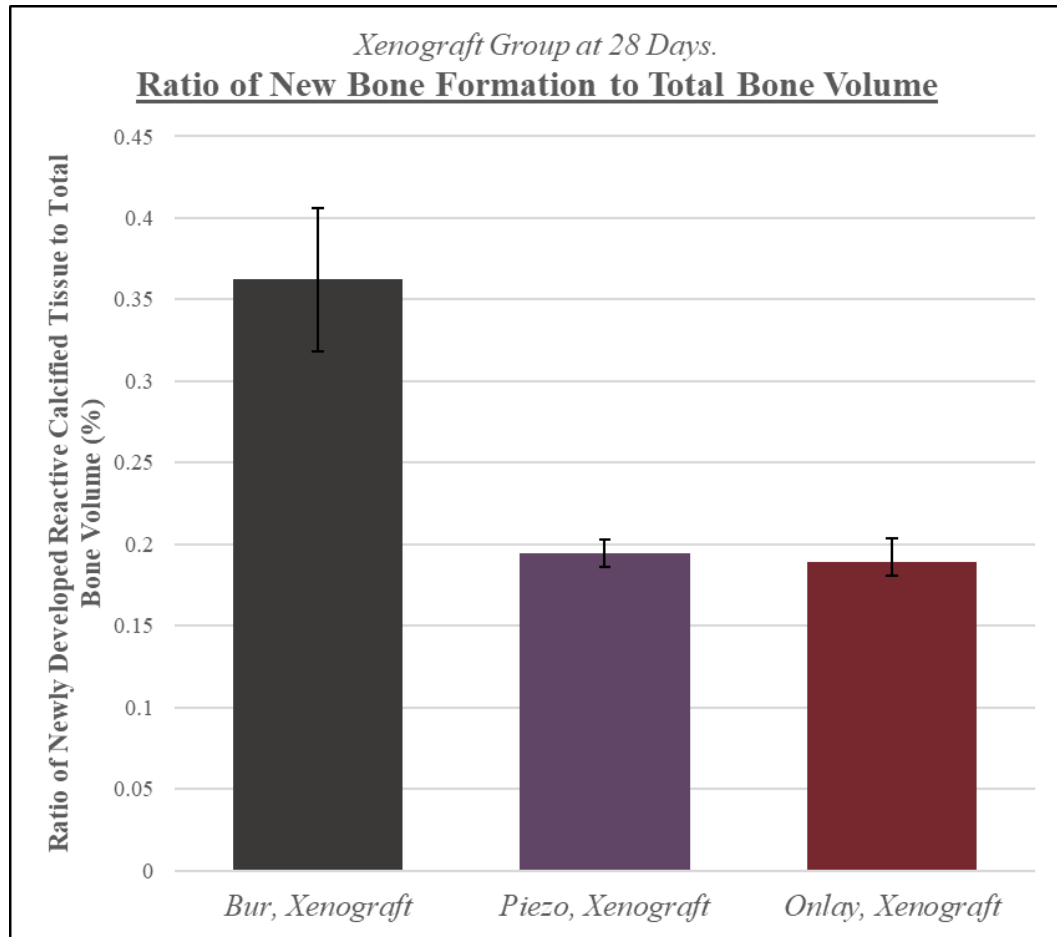
Figure 29. New bone formation data for the xenograft group at day 28.

This figure illustrates the new bone formation data for the 28-day *Xenograft* samples.

For our "*quantitative*" analysis of the new bone formation in the 28-day

Xenograft groups, selective cortical penetrations with a *Bur* yielded the highest

percentage of new bone formation to total bone volume. Analysis of variance (ANOVA)

was used with a power of 95% and a 5% critical level and showed no statistically

significant differences between the three groups (*Bur, Piezo, Onlay*).
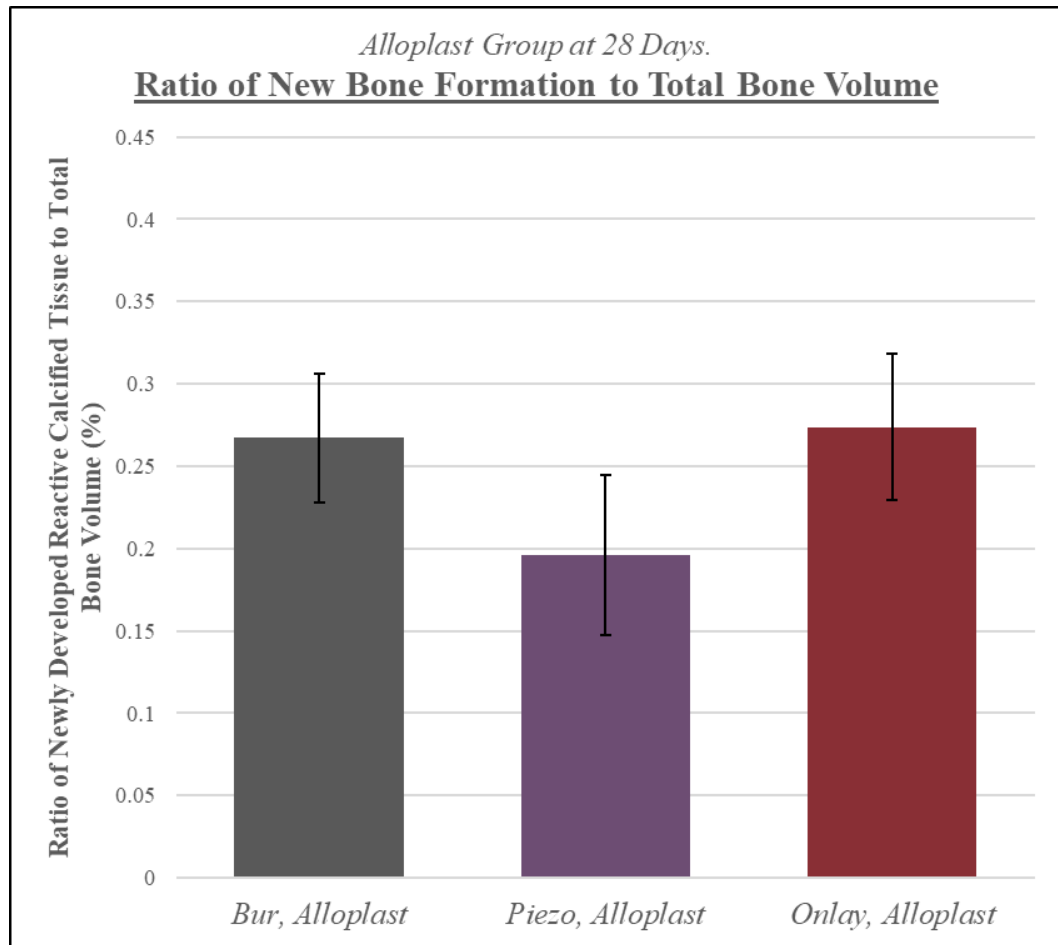
Figure 30. New bone formation data for the alloplast group at day 28.

This figure illustrates the new bone formation data for the 28-day *Alloplast* samples.

For our quantitative analysis of the new bone formation in the 28-day *Alloplast* groups, selective cortical penetrations with an *Onlay* technique yielded the highest percentage of new bone formation to total bone volume. ANOVA was used with a power of 95% and a 5% critical level and showed no statistically significant difference between the three groups (*Bur, Piezo, Onlay*).
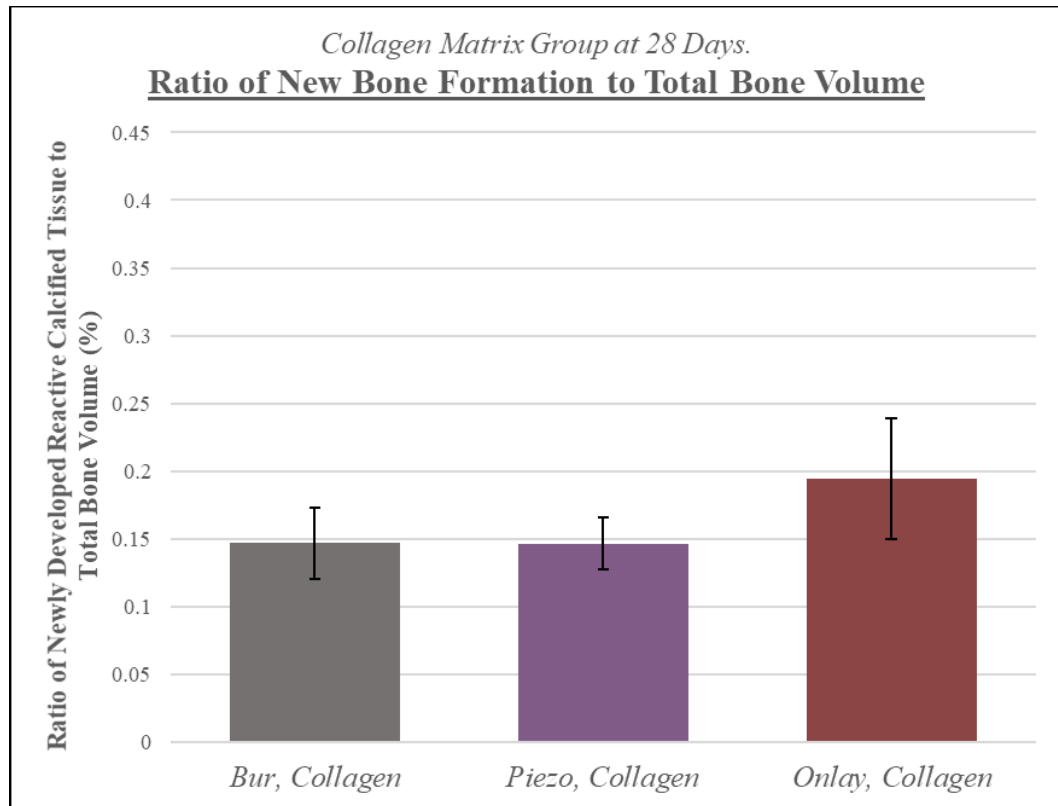
Figure 31. New bone formation data for the collagen matrix group at day 28.

This figure illustrates the new bone formation data for the 28-day *Collagen* samples.

For our quantitative analysis of the new bone formation in the 28-day *Collagen* groups, selective cortical penetrations with an *Onlay* technique yielded the highest percentage of new bone formation to total bone volume. ANOVA was used and again showed no statistically significant difference between the three groups (*Bur, Piezo, Onlay*), due to the small sample size.

Please note that we were able to include an extra surgical sample (*Piezo, Collagen*) into our project and we were able to obtain a μCT scan for one of these extra rat leg samples (*Sample #500L*). *See Appendix.* The sample was segmented using our deep learning algorithm and was included in the statistical analysis – therefore the *Piezo, Collagen* group contained 4 samples (*n=4*), whereas all other groups contained 3 samples (*n=3*).

3.1.3 Porosity Analysis
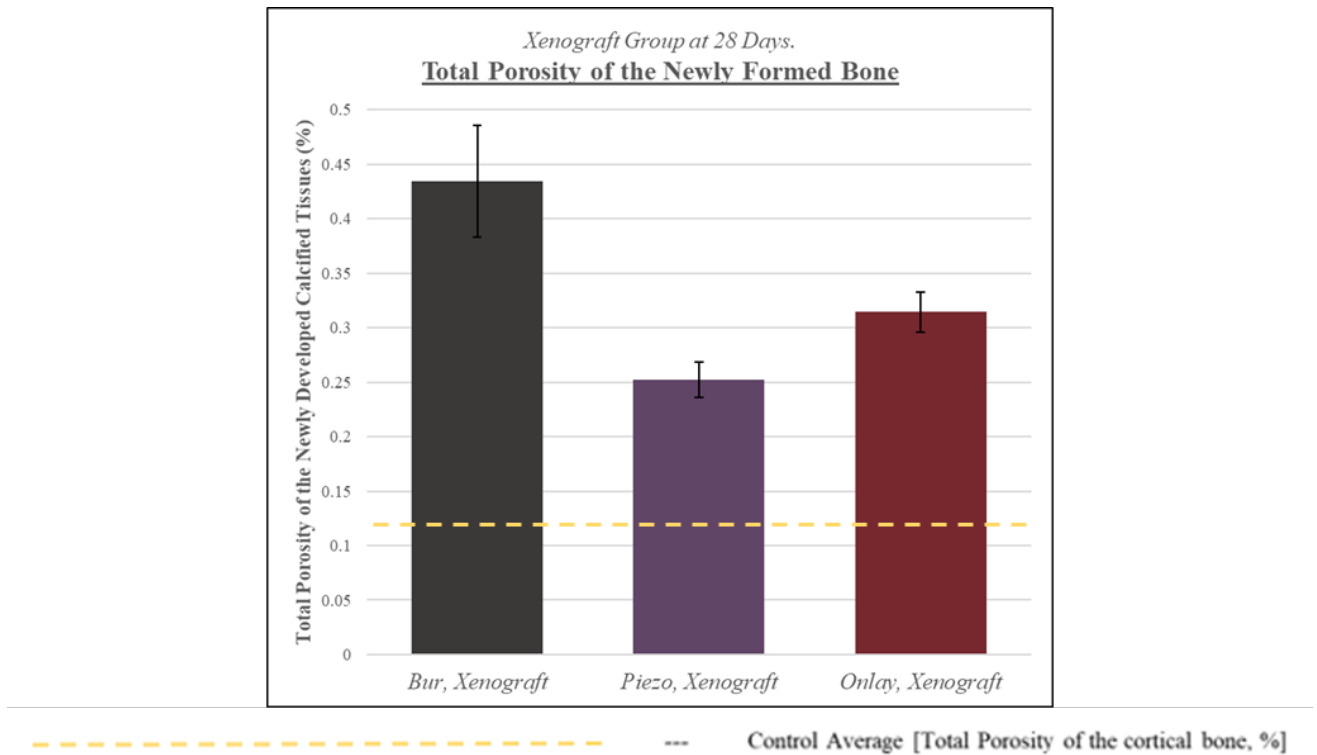
Figure 32. Total porosity data for the xenograft group at day 28.

This figure compares the data containing the total porosities of the new bone formation for the 28-day *Xenograft* samples.

For our "*qualitative*" analysis, the density of the newly formed bone was examined. In the 28-day *Xenograft* groups, selective cortical penetrations with a *Bur* yielded the highest total porosity of new bone formation. ANOVA was used and showed no statistically significant differences between the three groups (*Bur, Piezo, Onlay*). However, each experimental group displayed higher porosities relative to the *Control* group (yellow line in Figure 32).
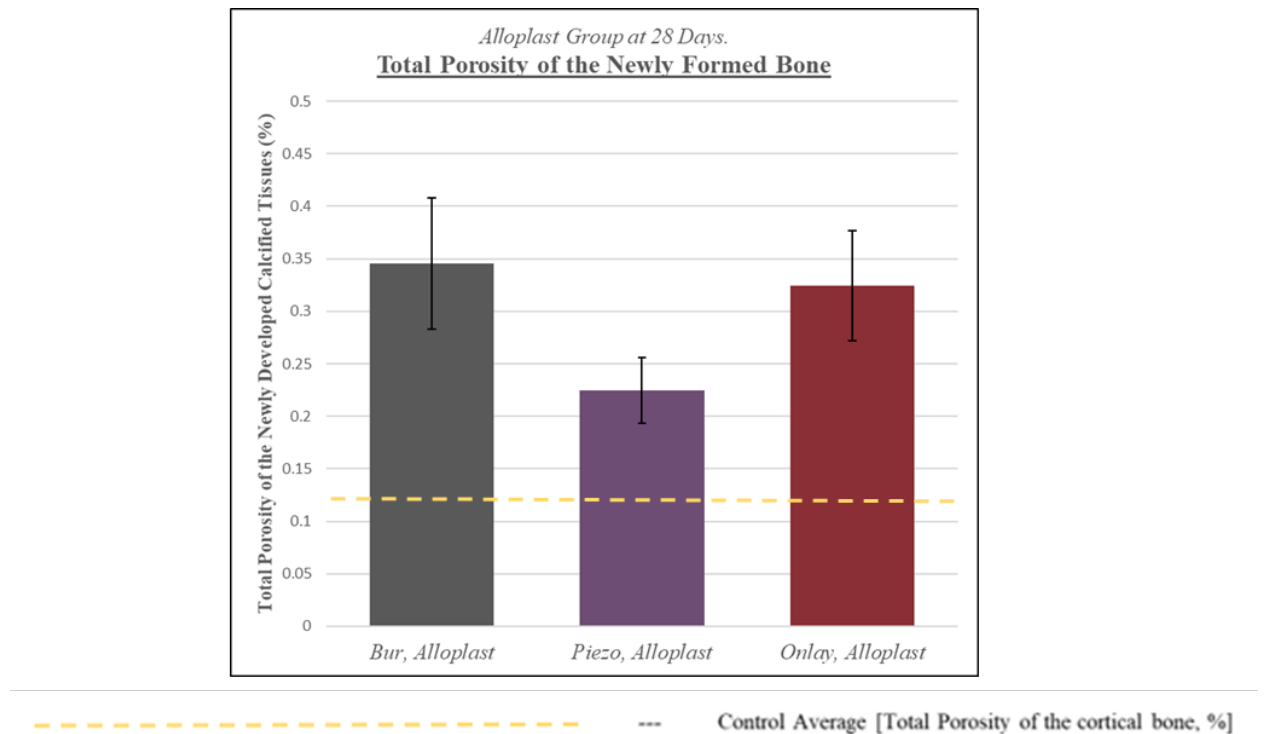
Figure 33. Total porosity data for the alloplast group at day 28.

This figure compares the data containing the total porosities of the new bone formation for the 28-day *Alloplast* samples.

For our qualitative analysis of the density of the newly formed bone in the 28-day *Alloplast* groups, again, selective cortical penetrations with a *Bur* yielded the highest total porosity of new bone formation. ANOVA was used and showed no statistically significant differences between the three groups (*Bur, Piezo, Onlay*). However, each experimental group displayed higher porosities relative to the *Control* group (yellow line in Figure 33).
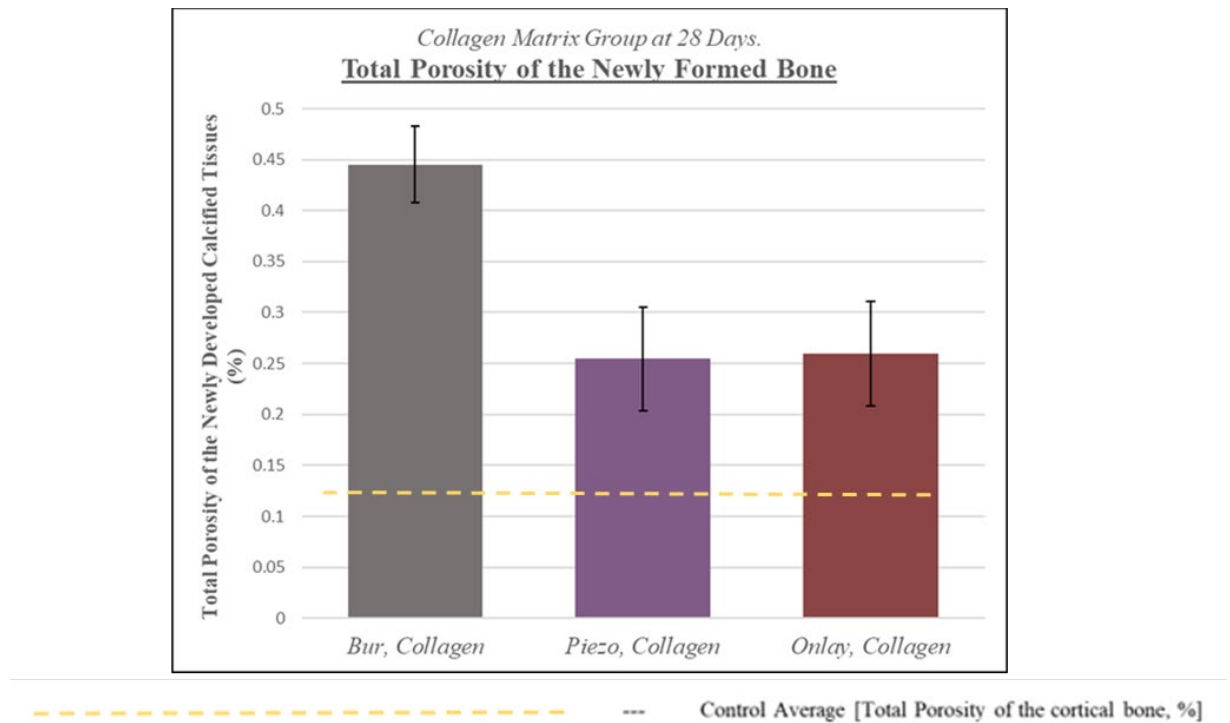
Figure 34. Total porosity data for the collagen matrix group at day 28.

This figure compares the data containing the total porosities of the new bone formation for the 28-day *Collagen* samples.

For our qualitative analysis of the density of the newly formed bone in the 28-day *Alloplast* groups, selective cortical penetrations with a *Bur* yielded the highest total porosity of new bone formation. ANOVA was used and showed no statistically significant differences between the three groups (*Bur, Piezo, Onlay*). Each experimental group displayed higher porosities relative to the *Control* group (yellow line in Figure 34).

Again, note that we were able to include an extra surgical sample (*Piezo, Collagen*) into our project and we were able to obtain a μCT scan for one of these extra rat leg sample (*Sample #500L*). The sample was segmented using our deep learning algorithm and was included in the statistical analysis – therefore the *Piezo, Collagen* group contained 4 samples (*n=4*), whereas all other groups contained 3 samples (*n=3*).

3.2 Hematological Analysis
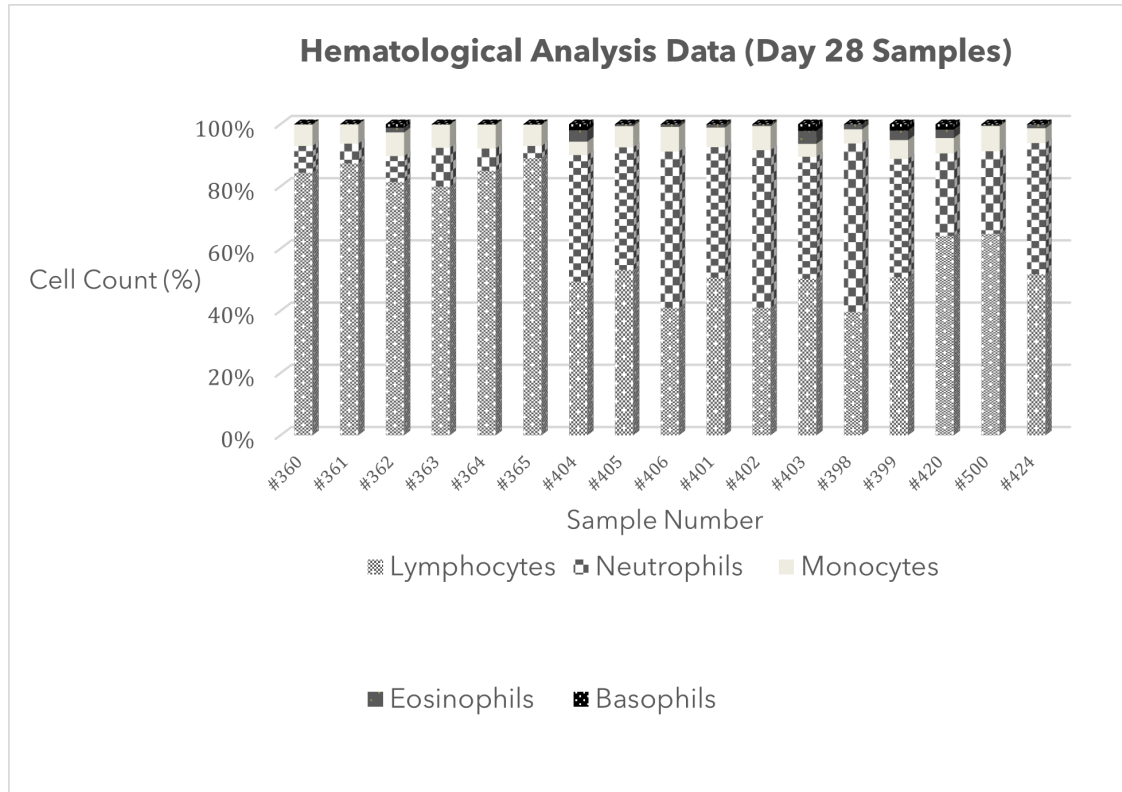
Figure 35. Differential white blood cell counts (%) at the time of sacrifice (day 28).

At day 28, no statistically significant differences were found in *lymphocyte* count, *neutrophil* count, *monocyte* count, *eosinophil* count, and *basophil* count when compared to the normal hematological range(s) in rodents.

3.3 Post-Operative Weight Monitoring Analysis
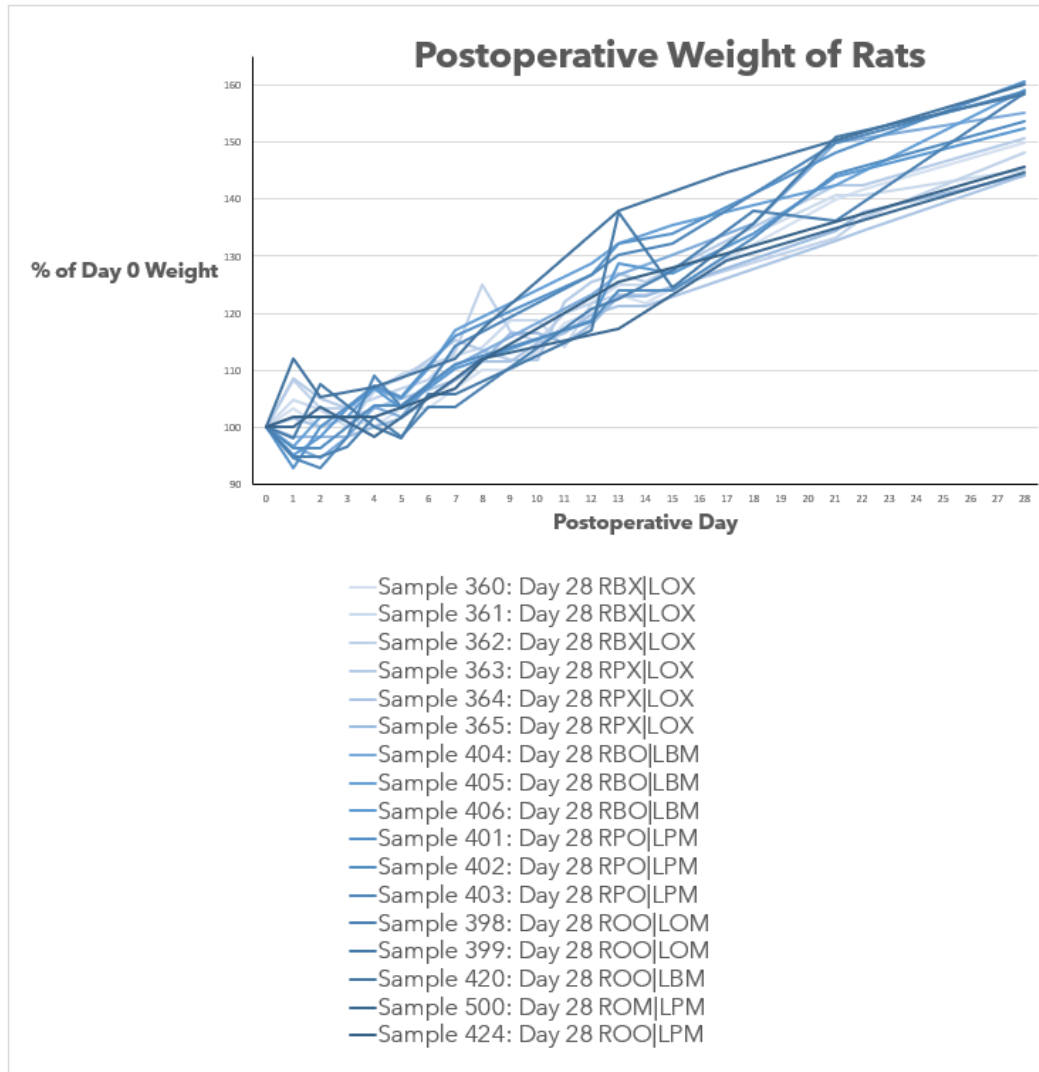
Figure 36. Graph of the post-operative weight in % of the original weight.

For the post-operative weights of the rats, the data was converted in % of the original weight and then ANOVA was calculated and there were no statistically significant differences between the samples.

CHAPTER 4

DISCUSSION

4.1 Imaging Analysis

The results from the present investigation show clear differences in hard tissue reaction and bone graft healing in response to the nine different surgical techniques tested, with or without the use of selective cortical penetrations. They also illustrate the power of microcomputed tomography and machine learning.

Sample preparation for histological processing is very challenging and when trying to isolate small regions of interest on the micron level, it can be difficult to keep the hard and soft tissues intact and sectioning may even lead to the inadvertent loss of valuable samples/data. Micro-computed tomography (μCT) is an increasingly useful tool for visualizing and analyzing three-dimensional structures. μCT scans typically contain 600-1,000 slices of data whereas histological sectioning may only yield one or two slices of interest. The 3D microscope (Xradia Versa 520, Zeiss) allowed us to obtain accurate, non-destructive images of our virtual samples and analyze thousands of slices of data at a very high resolution (10 μm).

While our μCT scans provided us with tens of thousands slices of data, it was a challenge to determine the best way of extracting meaningful data from the large samples. The small voxel size of our scans allowed us to visualize the porosities and intricacies of the cortical and trabecular bone in the rat tibia, however traditional

segmentation techniques were not accurate enough to extract useful data. First, traditional window-leveling and thresholding techniques were attempted to separate the new bone formation from the original cortical bone, the bone graft particles, the background, and the noise in our volumes. The contrasts in our high resolution µCT scans were not distinct enough for these methods because there were highly radio-opaque bone graft particles, cortical bone, and new bone matrix. There were distinct peaks distinguishing background from the highly mineralized tissues, however these techniques were not able to separate the volumes of interest for this study. Manually segmenting each slice of data would have required too much time and manpower so we turned to machine learning. And our convolution neural network (CNN) algorithm was very successful in identifying the original tibial diaphysis anatomy (based on our training input), the newly formed hard tissues, and the isolated bone graft particles. Our deep neural network algorithm allowed us to extract the most possible data from our µCT scans than previously thought possible. And, the model is flexible enough to be modified based on the requirements of each individual study design – yielding unbiased, reliable and accurate segmentations in a valid and reproducible way with relatively little manual inputs.

Also, the choice to not use a membrane in our study made this experiment feasible because stabilizing a membrane over our grafts in a rat tibia is extremely technique sensitive. And the results from this study (and others) showed that new bone growth can be achieved without the use of a cell occlusive membrane. When preparing our surgical sites, special care was taken to keep the periosteum intact, which allowed for

bone graft material stabilization under periosteum only and subsequent hard tissue formation in the graft site(s).

4.1.1 New Bone Formation

As mentioned previously, selective cortical penetrations are thought to increase the blood supply to the bone graft site(s), enhancing angiogenesis, bone healing, and integration of bone graft. However, the benefits of such techniques have not yet been proven in longitudinal human clinical trials. This study confirmed that selective cortical penetrations are not entirely necessary for new bone formation to occur (*Onlay* group). The SCP groups (*Bur, Piezo*) also yielded new bone formation.

The sample size in this study (*n=3*) was small and this was one of the limitations of this study. The resulting ratios of new bone formation to total bone volume were quite variable and there were no statistically significant differences found between the experimental groups. There were also no clear patterns in found when comparing all nine bone grafting techniques (Figure 37) except that the collagen matrix groups tended to show lower levels of new bone formation, perhaps because the collagen matrix used did not maintain the graft site volume long enough to allow for new bone formation. Interestingly though, the collagen matrix groups did yield new bone gain. Whether this is due to the grafting material, or the recipient site preparation is unclear.

A study by Goldman *et al.* [94] attributed part of this new bone formation in the outer surface of the bone to the disturbance of the periosteum alone. A combination of both the elevation of a full-thickness flap and the surgical procedures damages the bone structure and an increased response of the tissues would be expected. A recent histomorphometric study by Kernitsky *et al.* [95] showed that in a rat tibia model, full thickness flap reflection with or without selective cortical penetrations will yield an increased thickness of cortical bone by day 28 due to a deposition of new bone on the outer surface.

The present research also demonstrated that both xenogenic and alloplastic bone substitutes can be used successfully for bone grafting surgery. Figures 26 and 27 show new bone formation with both bone grafting materials and hard tissue encapsulated bone graft particles are present in our µCT scans. Dense, radiopaque calcifications (new bone formation) surrounded and were in intimate contact with the two bone substitute materials. When assessing the "quantity" of the new bone formation, measurements revealed no superior grafting material, perhaps due to the small sample size, but when assessing the "quality" of the newly formed bone, selective cortical penetrations (SCPs) with a piezoelectric knife yielded some interesting results.

An Overview of Each Group at 28 Days.
Ratio of New Bone Formation to Total Bone Volume
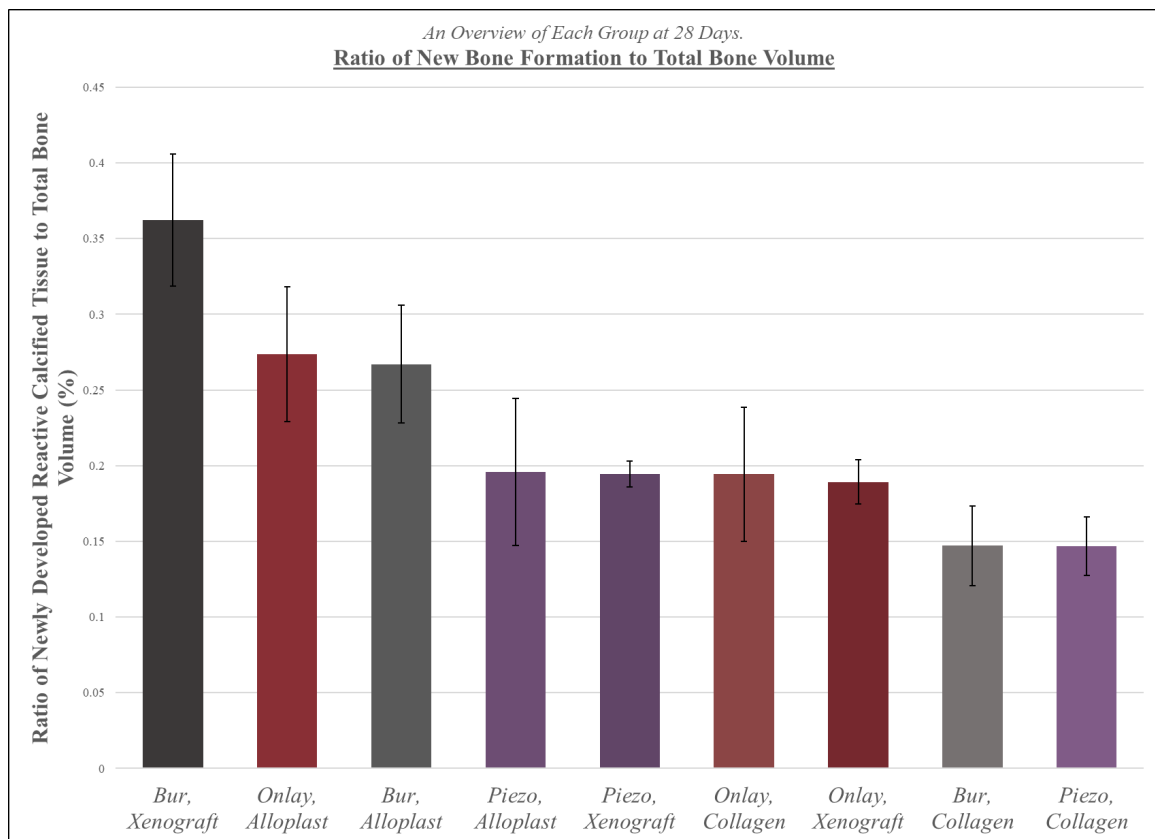
Figure 37. Ratio of New Bone Formation to Total Bone Volume Overview.

Figure 37 shows the new bone formation data for all 28-day samples in descending order. The *Bur, Xenograft* group yielded the highest ratio of new bone formation to total bone volume however there were no statistically significant differences between the groups. Each of the nine bone grafting techniques tested in this study did however result in new bone formation over the surgical site.

4.1.2 Total Porosity of Newly Formed Bone

The main clinical advantage of the piezoelectric knife is that it can cut hard

tissues and is generally safe to use adjacent to soft tissues. Although it does not cut the

soft tissues, it is still possible to induce direct damage with increased pressure or damage

from excessive overheating. Rashad *et al*., however showed that the heat produced by

rotary devices (*Bur*) is higher than that produced by ultrasonic devices (*Piezo*). [62]

Additionally, Anesi *et al.* [96] observed that both techniques induced osteocyte death

(RAP effect), but that the viable osteocytes were found significantly closer to the

osteotomy edge of piezosurgery samples, compared to conventional rotary bur. Findings

like this suggest that piezosurgery causes less damage to the bone and leads to a

difference physiological response. Whole scans of our experimental samples showed that,

for the *Piezo* and *Onlay* study groups, new bone formation was consistently found on one

side of the tibial diaphysis (the side where the SCPs were made, and the graft was

placed). Several, but not all, of our *Bur* samples however showed new bone formation not

only above graft site, but also on the adjacent side of the tibial diaphysis (*see Figure 26*

and Figure 27). This "undesirable" bone growth could be attributed to increased hard

tissue damage with a conventional bur.

The results of the present investigation showed that the porosities of the newly

formed bone varied depending on which surgical technique was used. (Figure 38) The

Control groups showed a uniformly dense cortical layer with little porosity and the

surgical sites in which selective cortical penetrations were made with a piezoelectric

knife (*Piezo*) showed dense, newly formed bone that was *not* statistically different from than that of the *Control* group. This phenomenon seems to be triggered by the specific ultrasonic vibrations and also has been shown to lead to bone hypermineralization. [97] This could be useful in periodontal surgery for implant site preparation, site development, and influencing the secondary stability of dental implants.
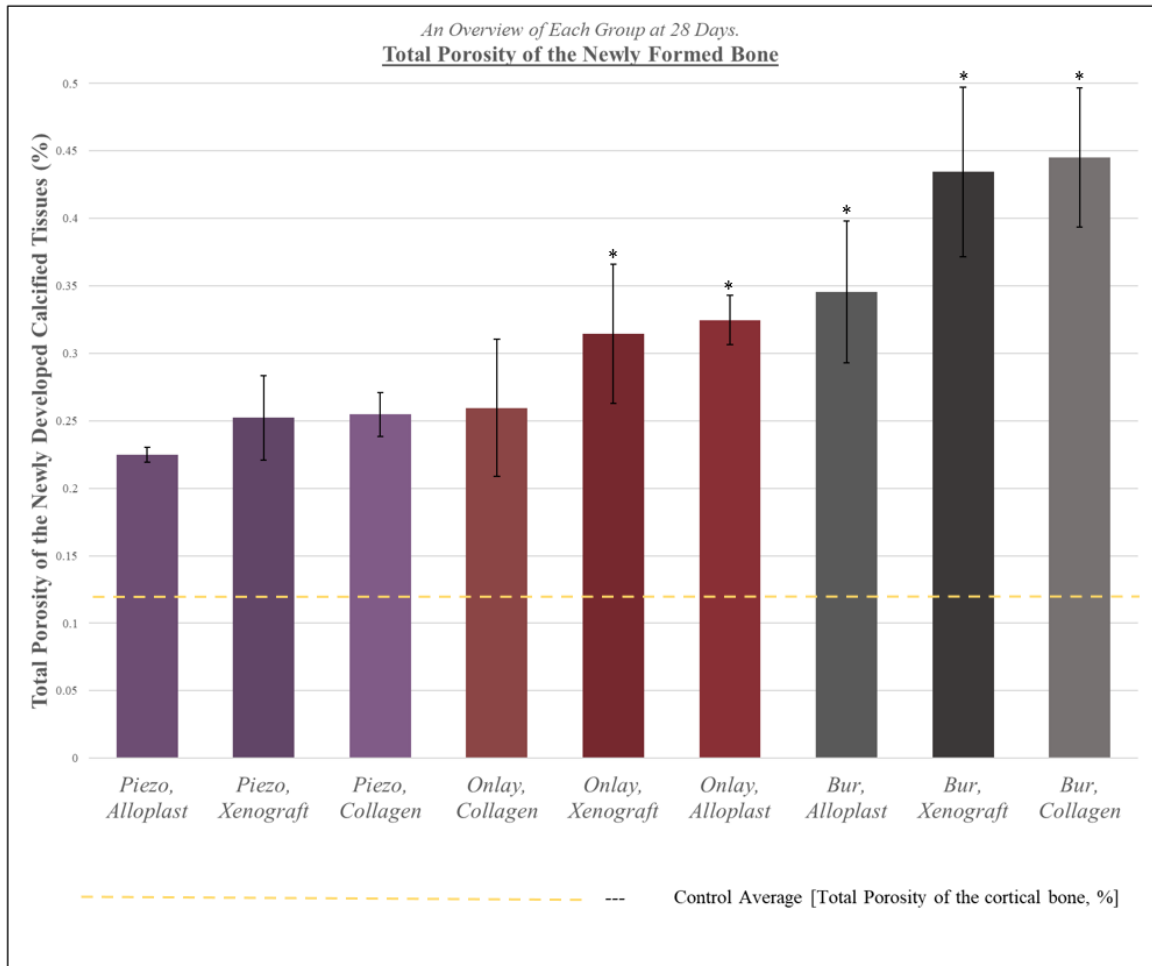
Figure 38. Total Porosity of the Newly Formed Bone Overview.

Figure 38 shows the total porosity data for all 28-day samples in ascending order. The Dunnett's test was used to compare total porosities to the control and unlike the other groups, the *Piezo* group was the only one that was consistently not statistically significant from the control. This result can be interpreted various ways, but it shows that the newly formed bone in sites in which SCPs are created with a piezoelectric knife is the most "cortical-like".

4.2 Hematological Analysis

No statistical differences were obtained in the white blood cell counts at day 28. This indicates that there were no hematological abnormalities throughout the post-operative healing period and that the effects of our bone grafting surgeries were not systemic.

4.3 Weight Analysis

No statistically significant differences in post-operative weights were found between the different samples during the 28 days of post-operative healing.

Daily behavioral assessments during the first two-post operative weeks revealed no abnormalities in food consumption, ambulation (physical activity), distress and overall behavior supporting the conclusion that healing was uneventful.

CHAPTER 5

CONCLUSION

Within the limitations of this study (mainly the small number of subjects), it is possible to conclude that the piezoelectric knife is a valid alternative to conventional carbide burs when making selective cortical penetrations prior to bone grafting surgery. Although this is a preliminary study, we have shown that new bone formation can be obtained with the three tested grafting materials: a xenogenic bone graft, an alloplast, and even a collagen matrix. We have also shown that bone augmentation can be achieved without the use of a cell occlusive membrane or without the use of selective cortical penetrations. The newly formed bone over sites with SCPs created with a piezoelectric knife, however, showed statistically significant different total porosities making the new bone formation in the *Piezo* groups more "cortical-like" at 28 days. This study also illustrated that deep learning, and the use of convolutional neural networks is a powerful tool capable of extracting enormous amounts of data from μCT volumes. The feature detection capabilities of our algorithm can be adapted for future projects and the applications of this advanced innovative technology are virtually endless. Another limitation of this study was the lack of histology. Due to delays caused by the COVID-19 pandemic, histological analysis was not feasible for this project and future studies should be conducted with histology, larger sample sizes, and more time points. Our preliminary study, though, was a great success which hopefully helped shed some light on the potential applications of deep learning in research and the piezoelectric knife in bone grafting surgeries.

28 DAY XENOGRAFT GROUP			Volume of Reactive Bone Formation [µm³]	Volume of Original Tibia Cortex [µm³]	Volume of Graft [µm³]	Total Volume [µm³]	Total Volume of Bone (Excluding Graft) [µm³]	Ratio of Reactive Calcified Tissue to Total Bone
BUR	#360 R.	ROI	15446251387	19974360773	6254039910	41674652071	35420612161	0.436080871
	#361 R.	ROI	12872152686	22345908519	8922772022	44140833227	35218061206	0.365498618
	#362 R.	ROI	8038332416	20183521285	8084899998	36306753700	28221853702	0.284826521
PIEZO	#363 R.	ROI	4771749742	22071400661	11319908057	38163058460	26843150403	0.177764147
	#364 R.	ROI	2,559,339,781.87	9,854,867,847.68	3650239779	16064447409	12414207630	0.206162154
	#365 R.	ROI	6392691085	25656315114	14707796497	46756802696	32049006199	0.199466125
ONLAY	#361 L.	ROI	11,460,795,125.93	54,385,177,876.23	21887436677	87733409679	65845973002	0.17405461
	#364 L.	ROI	8441419386	39663421740	20466719197	68571560323	48104841125	0.175479623
	#365 L.	ROI	12785652452	45756285445	18166228451	76708166348	58541937898	0.218401592

Figure 39. Volume Analysis Data for Day 28 Xenograft Samples.

28 DAY ALLOPLAST GROUP			Volume of Reactive Bone Formation [µm³]	Volume of Original Tibia Cortex [µm³]	Volume of Graft [µm³]	Total Volume [µm³]	Total Volume of Bone (Excluding Graft) [µm³]	Ratio of Reactive Calcified Tissue to Total Bone
BUR	#404 R.	ROI	3905028489	16210264382	807210364.8	20922503236	20115292871	0.194132321
	#405 R.	ROI	2,587,429,113.64	6,648,682,545.34	114396597.3	9350508256	9236111659	0.280142684
	#406 R.	ROI	9766420734	20093926102	934338096.4	30794684932	29860346835	0.327069903
PIEZO	#401 R.	ROI	8562783208	20640963701	901465105.9	30105212015	29203746909	0.293208376
	#402 R.	ROI	2,305,207,812.36	12,948,909,125.66	552351040.1	15806467978	15254116938	0.151120371
	#403 R.	ROI	3,305,632,226.79	19,782,955,986.61	466960003.8	23555548217	23088588213	0.143171691
ONLAY	#399 R.	ROI	9401430785	35400748429	1942530989	46744710203	44802179214	0.209843158
	#420 R.	ROI	19545400280	34834845102	2823135838	57203381220	54380245382	0.359420965
	#424 R.	ROI	12174384725	36087639462	1261542301	49523566489	48262024187	0.252255991

Figure 40. Volume Analysis Data for Day 28 Alloplast Samples.

28 DAY COLLAGEN GROUP			Volume of Reactive Bone Formation [µm³]	Volume of Original Tibia Cortex [µm³]	Volume of Graft [µm³]	Total Volume [µm³]	Total Volume of Bone (Excluding Graft) [µm³]	Ratio of Reactive Calcified Tissue to Total Bone
BUR	#404 L.	*ROI*	4382605632	21828836231	N/a	26211441862	26211441862	**0.167202005**
	#406 L.	*ROI*	6486520253	29717077898	N/a	36203598151	36203598151	**0.179167834**
	#420 L.	*ROI*	2356519097	22409073997	N/a	24765593094	24765593094	**0.095152944**
PIEZO	#401 L.	*ROI*	2791413559	15614419104	N/a	18405832663	18405832663	**0.151659184**
	#403 L.	*ROI*	2196520433	18648415161	N/a	20844935594	20844935594	**0.105374297**
	#424 L.	*ROI*	6322339846	25731132550	N/a	32053472396	32053472396	**0.197243524**
	#500 L.	*ROI*	3652904741	23895694550	N/a	27548599291	27548599291	**0.132598565**
ONLAY	#398 L.	*ROI*	3956896617	33303614715	N/a	37260511332	37260511332	**0.106195446**
	#399 L.	*ROI*	8,643,093,279.82	26,130,907,687.51	N/a	34774000967	34774000967	**0.248550441**
	#500 R.	*ROI*	11849210620	40070975033	N/a	51920185653	51920185653	**0.228219727**

Figure 41. Volume Analysis Data for Day 28 Collagen Samples.

28 DAY XENOGRAFT GROUP	Sample	Slice Number	Surface Area of New Bone [μm2]	Zone (ROI) of New Bone [μm2]	Density	Mean Density	Total Porosity
BUR		217	42,688,731.61	78,066,091.14	0.546828091		
		271	46,495,551.46	81,791,868.22	0.568461786		
		406	42,235,330.17	92,883,776.01	0.454711597		
	#360 R.	509	51,753,474.97	140,170,042.07	0.36921923	0.484805176	0.515194824
		197	67,924,223.76	121,080,660.14	0.560983263		
		251	62,249,328.38	131,126,887.07	0.474725892		
		352	64,336,455.17	117,783,759.62	0.546225179		
	#361 R.	450	48,967,936.19	78,884,607.48	0.620754007	0.550672085	0.449327915
		303	27,343,248.65	37,835,661.37	0.72268457		
		377	30,380,846.36	42,228,532.44	0.719438839		
		492	28,682,291.19	49,624,104.96	0.577991104		
	#362 R.	575	25,424,765.88	40,729,616.34	0.624232884	0.661086849	0.338913151
PIEZO		259	9,767,797.16	13,449,270.14	0.726269683		
		326	9,091,456.06	10,849,048.08	0.837995739		
		467	9,645,503.95	16,320,177.77	0.591017089		
	#363 R.	579	11,319,578.66	15,754,198.84	0.718511857	0.718448592	0.281551408
		38	14,646,987.62	19,097,594.53	0.766954581		
		178	15,131,984	20,617,304.34	0.733945804		
	#364 R.					0.750450192	0.249549808
		308	12,162,939.35	16,077,158.87	0.756535371		
		446	14,496,222.49	17,074,616.93	0.848992545		
		551	13,068,401.92	17,484,185.94	0.747441257		
	#365 R.	676	18,848,365.79	25,293,721.78	0.745179612	0.774537196	0.225462804
ONLAY		200	4,971,873.50	5,707,403.74	0.871127		
		400	7,388,338.11	8,854,540.40	0.834412378		
		600	24,643,663.79	43,323,411.31	0.568830179		
	#361 L.	800	21,312,887.48	34,748,702.76	0.6133434	0.721928239	0.278071761
		200	3,239,019.84	4,124,233.23	0.785362917		
		400	9,712,919.12	13,687,684.61	0.709610091		
		600	16,411,227.05	26,354,351.34	0.622714133		
	#364 L.	800	13,647,522.92	...257,978.53	0.540325225	0.664503091	0.335496909
		200	9,120,610.28	10,695,944.25	0.8527167		
		400	11,421,900.12	16,922,449.32	0.674955493		
		600	13,014,727.00	24,568,795.80	0.529725881		
	#365 L.	800	13,522,993.30	21,704,817.27	0.623041103	0.670109794	0.329890206

Figure 42. Density Analysis Data for Day 28 Xenograft Samples.

28 DAY ALLOPLAST GROUP	Sample	Slice Number	Surface Area of New Bone	Zone (ROI) of New Bone	Density	Mean Density	Total Porosity
BUR		58	14,539,694.31	17,832,706.45	0.815338622		
		160	13,489,867.28	16,071,375.55	0.839372289		
		264	13,839,467.88	18,512,428.44	0.747577117		
	#404 R.	356	13,536,002.25	19,083,476.93	0.709304824	0.777898213	0.222101787
		296	13,328,407.98	22,920,040.09	0.581517656		
		350	8,673,898.58	15,364,439.30	0.564543776		
	#405 R.					0.573030716	0.426969284
		304	25,558,686.49	41,559,836.34	0.614985254		
		395	27,462,089.92	41,696,589.64	0.658617171		
		496	23,457,750.51	37,748,977.53	0.621414196		
	#406 R.	610	18,854,735.51	33,900,638.18	0.556176418	0.61279826	0.38720174
PIEZO		537	16,999,580.25	22,190,237.64	0.76608374		
		640	17,626,755.14	24,840,786.09	0.709589265		
		741	18,562,958.03	24,380,790.30	0.761376387		
	#401 R.	847	22,949,129.38	32,113,583.04	0.714623758	0.737918287	0.262081713
		171	7,784,959.47	9,798,385.54	0.794514508		
		284	4,588,537.55	6,437,778.67	0.712751678		
		381	7,022,795.60	8,859,074.75	0.792723371		
	#402 R.	492	9,541,738.53	13,585,873.32	0.702327948	0.750579376	0.249420624
		326	7,056,326.84	8,366,657.24	0.843386628		
		416	4,375,875.24	4,882,576.87	0.896222498		
		506	3,425,302.99	4,148,872.91	0.825598437		
	#403 R.	614	5,332,527.91	6,810,069.85	0.783035714	0.837060819	0.162939181
ONLAY		200	12,753,644.04	16,175,748.63	0.788442274		
		400	5,775,750.97	6,650,772.68	0.868433075		
		600	8,122,308.04	11,354,014.40	0.715368834		
	#399 R.	800	17,294,844.69	29,354,750.45	0.58916681	0.740352748	0.259647252
		150	28,222,140.49	48,305,405.45	0.584243942		
		350	33,902,334.37	60,683,476.62	0.558674886		
		550	32,257,453.89	57,521,574.02	0.56078879		
	#420 R.	750	21,071,575.51	36,140,719.52	0.583042501	0.57168753	0.42831247
		275	14,892,586.00	23,478,736.58	0.634300996		
		400	15,601,515.63	22,369,768.08	0.697437523		
		525	15,003,989.23	21,127,115.72	0.710176885		
	#424 R.	650	17,961,238.54	22,013,277.76	0.815927493	0.714460724	0.285539276

Figure 43. Density Analysis Data for Day 28 Alloplast Samples.

28 DAY COLLAGEN GROUP	Sample	Slice Number	Surface Area of New Bone	Zone (ROI) of New Bone	Density	Mean Density	Total Porosity
BUR		275	5,350,988.64	8,110,598.88	0.65975259		
		384	6,885,344.09	10,606,713.47	0.64914963		
		537	8,457,197.01	16,381,322.04	0.51627073		
	#404 L.	644	8,786,566.57	13,022,765.91	0.67470817	0.624970279	0.375029721
		247	10,246,558.30	16,628,746.64	0.61619547		
		396	6,897,910.50	12,378,344.97	0.55725628		
		526	5,967,786.85	11,703,549.38	0.50991256		
	#406 L.	667	7,822,968.12	16,230,556.45	0.48199014	0.541338612	0.458661388
		270	4,977,644.91	10,213,028.00	0.48738189		
		387	5,967,677.11	11,378,346.59	0.52447665		
		512	7,906,210.23	15,303,051.64	0.51664272		
	#420 L.	638	8,584,757.90	18,526,611.13	0.46337443	0.497968924	0.502031076
PIEZO		38	6,119,647.23	7,613,873.75	0.8037495		
		144	5,897,942.89	7,553,132.83	0.78086048		
		237	4,338,926.06	6,077,128.59	0.71397635		
	#401 L.	332	6,159,128.82	8,054,445.79	0.76468686	0.765818294	0.234181706
		166	3,508,567.94	3,768,724.30	0.93096965		
		256	4,066,335.09	5,065,457.00	0.80275779		
		355	3,432,646.82	3,915,505.13	0.87668046		
	#403 L.	460	3,341,541.48	3,793,019.06	0.88097144	0.872844836	0.127155164
		274	15,512,043.09	24,879,651.21	0.62348314		
		392	17,114,252.05	25,425,536.57	0.67311272		
		503	13,797,416.19	21,360,031.22	0.64594551		
	#424 L.	605	14,198,704.08	24,630,508.73	0.57646816	0.629752382	0.370247618
		284	10,620,778.61	16,183,850.69	0.65625782		
		399	7,833,672.41	9,837,917.75	0.79627342		
		483	5,586,365.48	7,704,039.56	0.7251216		
	#500 L.	591	3,240,821.16	4,811,606.67	0.67354241	0.712798813	0.287201187
ONLAY		100	5,595,524.66	6,663,731.40	0.83969841		
		300	3,732,170.17	4,311,055.21	0.8657208		
		500	10,722,480.11	13,448,700.98	0.79728742		
	#398 L.	700	6,092,492.01	7,287,398.11	0.83603118	0.834684452	0.165315548
		200	20,944,319.90	25,835,924.49	0.81066655		
		400	23,109,525.49	32,788,748.70	0.70480047		
		600	20,183,460.84	26,387,285.48	0.76489341		
	#399 L.	800	14,133,692.95	22,160,860.26	0.63777727	0.729534427	0.270465573
		100	31,914,922.70	39,191,739.72	0.81432779		
		300	20,156,793.28	29,423,167.21	0.68506538		
		500	14,107,122.80	23,731,920.72	0.59443662		
	#500 R.	700	15,079,120.07	28,182,320.14	0.53505602	0.657221453	0.342778547

Figure 44. Density Analysis Data for Day 28 Collagen Samples.

28 DAY CONTROL GROUP	Sample	Slice Number	Surface Area of Original Bone	Zone (ROI) of Cortical Bone	Density	Mean Density	Total Porosity
CONTROL	#359 L.	100	38,890,346.63	41,670,556.40	0.933281194		
		300	36,872,196.99	41,262,114.10	0.893609011		
		500	33,730,450.30	40,860,981.73	0.8254929		
		700	35,469,908.89	40,777,222.12	0.869846131		
		900	35,470,822.63	41,253,890.43	0.859817638	0.876409375	0.123590625
	#355 R.	100	27,432,390.83	31,120,068.45	0.881501622		
		300	28,778,685.84	31,268,679.52	0.920367802		
		500	26,425,475.00	30,875,618.40	0.855868688		
		700	26,891,021.93	31,175,266.85	0.862575517		
		900	28,265,219.42	32,466,363.45	0.870600105	0.878182747	0.121817253
	#395 L.	100	33,654,877.72	38,959,602.93	0.863840368		
		300	33,826,685.75	38,502,971.31	0.878547411		
		500	34,527,930.58	36,953,652.80	0.934357715		
		700	32,969,168.73	36,631,055.81	0.900033264	0.894194689	0.105805311

Figure 45. Density Analysis Data for Day 28 Control Samples.

Sample Group	Sample Number	Sample Label	Neutrophils (%)	Lymphocytes (%)	Monocytes (%)	Eosinophils (%)	Basophils (%)
Day 28 Samples: Xenograft	360	Day 28 RBX|LOX	8.59	84.43	6.86	0.09	0.02
	361	Day 28 RBX|LOX	6.36	87.41	6.19	0	0.05
	362	Day 28 RBX|LOX	8.31	81.45	7.64	1.5	1.1
	363	Day 28 RPX|LOX	12.47	79.96	7.45	0.06	0.06
	364	Day 28 RPX|LOX	7.13	85.05	7.67	0.14	0
	365	Day 28 RPX|LOX	3.91	89.13	6.82	0.1	0.05
Day 28 Samples: Alloplast and Collagen	404	Day 28 RBO|LBM	40.67	49.41	4.31	3.68	1.92
	405	Day 28 RBO|LBM	39.38	53.19	6.81	0.57	0.05
	406	Day 28 RBO|LBM	50.28	40.96	7.92	0.79	0.06
	401	Day 28 RPO|LPM	41.93	50.7	6.32	0.96	0.1
	402	Day 28 RPO|LPM	50.63	41.04	7.73	0.51	0.09
	403	Day 28 RPO|LPM	39.21	50.36	4.14	4.17	2.14
	398	Day 28 ROO|LOM	54.14	39.68	4.57	1.56	0.05
	399	Day 28 ROO|LOM	38.07	50.8	6.04	3.05	2.04
	420	Day 28 ROO|LBM	26.55	64.07	4.95	2.7	1.73
	500	Day 28 ROM|LPM	26.54	64.79	8.1	0.3	0.28
	424	Day 28 ROO|LPM	42.17	51.78	4.75	1.18	0.12

Figure 46. Hematology Data for Day 28 Experimental Samples.

Day 28 Samples: Xenograft (Weight, g)

Sample	360	361	362	363	364	365
Description	Day 28 RBXILOX	Day 28 RBXILOX	Day 28 RBXILOX	Day 28 RPXILOX	Day 28 RPXILOX	Day 28 RPXILOX
Day 0	300	320	300	295	305	305
Day 1	310	335	325	320	310	300
Day 2	300	330	310	310	305	300
Day 3	305	320	310	305	310	300
Day 4	300	340	315	315	315	305
Day 5	310	350	320	320	320	310
Day 6	310	355	325	330	325	320
Day 7	320	360	340	340	330	330
Day 8	330	365	375	335	340	340
Day 9	330	380	350	330	340	355
Day 10	340	380	345	330	350	355
Day 11	355	365	360	360	355	350
Day 12	360	390	365	370	365	360
Day 13	370	400	370	375	370	375
Day 14	365	400	370	370	370	375
Day 15						
Day 16						
Day 17						
Day 18						
Day 19						
Day 20						
Day 21	420	450	400	420	405	410
Day 22	425	450	410	420	410	420
Day 23						
Day 24						
Day 25						
Day 26						
Day 27						
Day 28	450	465	445	445	440	440

Day 28 Samples: Alloplast and Collagen (Weight, g)

Sample	404	405	406	401	402	403	398	399	420	500	424
Description	Day 28 RBOILBM	Day 28 RBOILBM	Day 28 RBOILBM	Day 28 RPOLPM	Day 28 RPOLPM	Day 28 RPOLPM	Day 28 ROOILOM	Day 28 ROOILOM	Day 28 ROOILBM	Day 28 ROMILPM	Day 28 ROOILPM
Day 0	280	295	295	280	270	280	290	265	290	290	295
Day 1	270	285	280	260	260	265	275	260	325	290	300
Day 2	255	300	290	280	260	260	275	285	305	300	300
Day 3	275	300	305	290	270	275	280	275			
Day 4	290	315	315	300	280	305	295	265	310	285	300
Day 5	285	310	305	295	280	290	285	260			
Day 6	300	325	315	310	290	300	300	280			
Day 7	310	345	325	325	300	320	300	280	325	315	315
Day 8									340	325	330
Day 9											
Day 10											
Day 11											
Day 12	345	380	350	355	320	355	350	310			370
Day 13	355	390	380	370	335	365	355	365	400	340	
Day 14											
Day 15	365	400	375	375	335	370	370	330			
Day 16											
Day 17									420	375	385
Day 18	380	410	395	395	360	395	400	360			
Day 19											
Day 20											
Day 21	420	420	425	415	390	420	395	400			
Day 22											
Day 23											
Day 24											
Day 25											
Day 26											
Day 27											
Day 28	435	470	450	450	415	445	460	420	465	420	430

Figure 47. Weight Data for Day 28 Experimental Samples.

BIBLIOGRAPHY

[1] Danesh-Sani, S. A., Tarnow, D., Yip, J. K., & Mojaver, R. (2017). The influence of cortical bone perforation on guided bone regeneration in humans. *International journal of oral and maxillofacial surgery*, *46*(2), 261–266.

[2] Greenstein, G., Greenstein, B., Cavallaro, J., & Tarnow, D. (2009). The role of bone decortication in enhancing the results of guided bone regeneration: a literature review. *Journal of periodontology*, *80*(2), 175–189.

[3] Adeyemo, W. L., Reuther, T., Bloch, W., Korkmaz, Y., Fischer, J. H., Zöller, J. E., & Kuebler, A. C. (2008). Influence of host periosteum and recipient bed perforation on the healing of onlay mandibular bone graft: an experimental pilot study in the sheep. *Oral and maxillofacial surgery*, *12*(1), 19–28.

[4] Aghaloo, T. L., & Moy, P. K. (2007). Which hard tissue augmentation techniques are the most successful in furnishing bony support for implant placement?. *The International journal of oral & maxillofacial implants*, 22 Suppl, 49–70.

[5] Marx R. E. (2007). Bone and bone graft healing. *Oral and maxillofacial surgery clinics of North America*, *19*(4), 455–v.

[6] Albrektsson, T., & Johansson, C. (2001). Osteoinduction, osteoconduction and osseointegration. *European spine journal : official publication of the European Spine Society, the European Spinal Deformity Society, and the European Section of the Cervical Spine Research Society*, 10 Suppl 2(Suppl 2), S96–S101.

[7] Wilson-Hench J (1987) Osteoinduction. *Progress in Biomedical Engineering: Definitions in Biomaterials (Williams D, ed), Elsevier, Amsterdam*, pp 29.

[8] Bauer, T. W., & Muschler, G. F. (2000). Bone graft materials. An overview of the basic science. *Clinical orthopaedics and related research*, (371), 10–27.

[9] Roberts, T. T., & Rosenbaum, A. J. (2012). Bone grafts, bone substitutes and orthobiologics: the bridge between basic science and clinical advancements in fracture healing. *Organogenesis*, *8*(4), 114–124.

[10] Precheur H. V. (2007). Bone graft materials. *Dental clinics of North America*, *51*(3), 729–viii.

[11] Griffin SK, Davis MK, McKinley OT, Anglen OJ, Chu GT, Boerckel DJ, Kacena AM, (2015) Evolution of Bone Grafting: Bone Grafts and Tissue Engineering Strategies for Vascularized Bone Regeneration, *Clinical Reviews in Bone and Mineral Metabolism*, 13, 232–244.

[12] Sanz, M., Dahlin, C., Apatzidou, D., Artzi, Z., Bozic, D., Calciolari, E., De Bruyn, H., Dommisch, H., Donos, N., Eickholz, P., Ellingsen, J. E., Haugen, H. J., Herrera, D., Lambert, F., Layrolle, P., Montero, E., Mustafa, K., Omar, O., & Schliephake, H. (2019). Biomaterials and regenerative technologies used in bone regeneration in the craniomaxillofacial region: Consensus report of group 2 of the 15th European Workshop on Periodontology on Bone Regeneration. *Journal of clinical periodontology*, 46 Suppl 21, 82–91.

[13] Mardas, N., Chadha, V., & Donos, N. (2010). Alveolar ridge preservation with guided bone regeneration and a synthetic bone substitute or a bovine-derived xenograft: a randomized, controlled clinical trial. *Clinical oral implants research*, *21*(7), 688–698.

[14] Mardas, N., D'Aiuto, F., Mezzomo, L., Arzoumanidi, M., & Donos, N. (2011). Radiographic alveolar bone changes following ridge preservation with two different biomaterials. *Clinical oral implants research*, *22*(4), 416–423.

[15] Patel, K., Mardas, N., & Donos, N. (2013). Radiographic and clinical outcomes of implants placed in ridge preserved sites: a 12-month post-loading follow-up. *Clinical oral implants research*, *24*(6), 599–605.

[16] Guarnieri, R., Belleggia, F., DeVillier, P., & Testarelli, L. (2018). Histologic and Histomorphometric Analysis of Bone Regeneration with Bovine Grafting Material after 24 Months of Healing. A Case Report. *Journal of functional biomaterials*, *9*(3), 48.

[17] Wang, W., & Yeung, K. (2017). Bone grafts and biomaterials substitutes for bone defect repair: A review. *Bioactive materials*, *2*(4), 224–247.

[18] Haugen, H. J., Lyngstadaas, S. P., Rossi, F., & Perale, G. (2019). Bone grafts: which is the ideal biomaterial?. *Journal of clinical periodontology*, *46 Suppl 21*, 92–102.

[19] Fuchs, J. R., Nasseri, B. A., & Vacanti, J. P. (2001). Tissue engineering: a 21st century solution to surgical reconstruction. *The Annals of thoracic surgery*, *72*(2), 577–591.

[20] Kretlow, J. D., & Mikos, A. G. (2007). Review: mineralization of synthetic polymer scaffolds for bone tissue engineering. *Tissue engineering*, *13*(5), 927–938.

[21] Valen, M., & Ganz, S. D. (2002). A synthetic bioactive resorbable graft for predictable implant reconstruction: part one. *The Journal of oral implantology*, *28*(4), 167–177.

[22] Vlassis, J. M., Hurzeler, M. B., & Quinones, C. R. (1993). Sinus lift augmentation to facilitate placement of nonsubmerged implants: a clinical and histological report. *Practical periodontics and aesthetic dentistry : PPAD*, *5*(2), 15–24.

[23] Fugazzotto, P. A., & Vlassis, J. (1998). Long-term success of sinus augmentation using various surgical approaches and grafting materials. *The International journal of oral & maxillofacial implants*, *13*(1), 52–58.

[24] Stevens, M. M., Marini, R. P., Schaefer, D., Aronson, J., Langer, R., & Shastri, V. P. (2005). In vivo engineering of organs: the bone bioreactor. *Proceedings of the National Academy of Sciences of the United States of America*, *102*(32), 11450–11455.

[25] Ghanaati, S., Schlee, M., Webber, M. J., Willershausen, I., Barbeck, M., Balic, E., Görlach, C., Stupp, S. I., Sader, R. A., & Kirkpatrick, C. J. (2011). Evaluation of the tissue reaction to a new bilayered collagen matrix in vivo and its translation to the clinic. *Biomedical materials (Bristol, England)*, *6*(1), 015010.

[26] Sanz, M., Lorenzo, R., Aranda, J. J., Martin, C., & Orsini, M. (2009). Clinical evaluation of a new collagen matrix (Mucograft prototype) to enhance the width of keratinized tissue in patients with fixed prosthetic restorations: a randomized prospective clinical trial. *Journal of clinical periodontology*, *36*(10), 868–876.

[27] Rotundo, R., & Pini-Prato, G. (2012). Use of a new collagen matrix (mucograft) for the treatment of multiple gingival recessions: case reports. *The International journal of periodontics & restorative dentistry*, *32*(4), 413–419.

[28] Chin, M., & Toth, B. A. (1996). Distraction osteogenesis in maxillofacial surgery using internal devices: review of five cases. *Journal of oral and maxillofacial surgery : official journal of the American Association of Oral and Maxillofacial Surgeons*, *54*(1), 45–54.

[29] Yamauchi, K., Takahashi, T., Nogami, S., Kataoka, Y., Miyamoto, I., & Funaki, K. (2013). Horizontal alveolar distraction osteogenesis for dental implant: long-term results. *Clinical oral implants research*, *24*(5), 563–568.

[30] Mohanty, R., Kumar, N. N., & Ravindran, C. (2015). Vertical Alveolar Ridge Augmentation by Distraction Osteogenesis. *Journal of clinical and diagnostic research : JCDR*, *9*(12), ZC43–ZC46.

[31] Scipioni, A., Bruschi, G. B., & Calesini, G. (1994). The edentulous ridge expansion technique: a five-year study. *The International journal of periodontics & restorative dentistry*, *14*(5), 451–459.

[32] Simion, M., Baldoni, M., & Zaffe, D. (1992). Jawbone enlargement using immediate implant placement associated with a split-crest technique and guided tissue regeneration. *The International journal of periodontics & restorative dentistry*, *12*(6), 462–473.

[33] Summers R. B. (1994). The osteotome technique: Part 2--The ridge expansion osteotomy (REO) procedure. *Compendium (Newtown, Pa.)*, *15*(4), 422–436.

[34] Tatum H., Jr (1986). Maxillary and sinus implant reconstructions. *Dental clinics of North America*, *30*(2), 207–229.

[35] Boyne PJ, James RA. Grafting of the maxillary sinus floor with autogenous marrow and bone. *Journal of Oral Surgery.* 1980;38(8):613–616.

[36] Summers R. B. (1994). A new concept in maxillary implant surgery: the osteotome technique. *Compendium (Newtown, Pa.)*, *15*(2), 152–162.

[37] Pinchasov, G., & Juodzbalys, G. (2014). Graft-free sinus augmentation procedure: a literature review. *Journal of oral & maxillofacial research*, *5*(1), e1.

[38] Yan, M., Liu, R., Bai, S., Wang, M., Xia, H., & Chen, J. (2018). Transalveolar sinus floor lift without bone grafting in atrophic maxilla: A meta-analysis. *Scientific reports*, *8*(1), 1451.

[39] Ceccarelli, G., Graziano, A., Benedetti, L., Imbriani, M., Romano, F., Ferrarotti, F., Aimetti, M., & Cusella de Angelis, G. M. (2016). Osteogenic Potential of Human Oral-Periosteal Cells (PCs) Isolated From Different Oral Origin: An In Vitro Study. *Journal of cellular physiology*, *231*(3), 607–612.

[40] Kent, J. N., Quinn, J. H., Zide, M. F., Guerra, L. R., & Boyne, P. J. (1983). Alveolar ridge augmentation using nonresorbable hydroxylapatite with or without autogenous cancellous bone. *Journal of oral and maxillofacial surgery : official journal of the American Association of Oral and Maxillofacial Surgeons*, *41*(10), 629–642.

[41] Block, M. S., & Degen, M. (2004). Horizontal ridge augmentation using human mineralized particulate bone: preliminary results. *Journal of oral and maxillofacial surgery : official journal of the American Association of Oral and Maxillofacial Surgeons*, *62*(9 Suppl 2), 67–72.

[42] Hasson O. (2007). Augmentation of deficient lateral alveolar ridge using the subperiosteal tunneling dissection approach. *Oral surgery, oral medicine, oral pathology, oral radiology, and endodontics*, *103*(3), e14–e19.

[43] Dibart, S., Sebaoun, J. D., & Surmenian, J. (2009). Piezocision: a minimally invasive, periodontally accelerated orthodontic tooth movement procedure. *Compendium of continuing education in dentistry (Jamesburg, N.J. : 1995)*, *30*(6), 342–350.

[44] Nevins, M. L., Camelo, M., Nevins, M., Schupbach, P., Friedland, B., Camelo, J. M., & Kim, D. M. (2009). Minimally invasive alveolar ridge augmentation procedure (tunneling technique) using rhPDGF-BB in combination with three matrices: a case series. *The International journal of periodontics & restorative dentistry*, *29*(4), 371–383.

[45] Kim, H. S., Kim, Y. K., & Yun, P. Y. (2016). Minimal invasive horizontal ridge augmentation using subperiosteal tunneling technique. *Maxillofacial plastic and reconstructive surgery*, *38*(1), 41.

[46] Lee E. A. (2017). Subperiosteal Minimally Invasive Aesthetic Ridge Augmentation Technique (SMART): A New Standard for Bone Reconstruction of the Jaws. *The International journal of periodontics & restorative dentistry*, *37*(2), 165–173.

[47] Lee E. A. (2017). Tridimensional Reconstruction of a Complex Iatrogenic Defect Using Orthodontic Forced Eruption and Minimally Invasive Bone Grafting. *Compendium of continuing education in dentistry (Jamesburg, N.J. : 1995)*, *38*(7), 447–456.

[48] Kakar, A., Kakar, K., Sripathi Rao, B. H., Lindner, A., Nagursky, H., Jain, G., & Patney, A. (2018). Lateral alveolar ridge augmentation procedure using subperiosteal tunneling technique: a pilot study. *Maxillofacial plastic and reconstructive surgery*, *40*(1), 3.

[49] Yamauchi, K., Imoto, K., Odajima, K., Morishima, H., Shimizu, Y., Nogami, S., & Takahashi, T. (2022). A collagen membrane for periosteal expansion osteogenesis using a timed-release system in rabbit calvaria. *International journal of implant dentistry*, *8*(1), 9.

[50] Rompen, E. H., Biewer, R., Vanheusden, A., Zahedi, S., & Nusgens, B. (1999). The influence of cortical perforations and of space filling with peripheral blood on the kinetics of guided bone generation. A comparative histometric study in the rat. *Clinical oral implants research*, *10*(2), 85–94.

[51] Wessing, B., Lettner, S., & Zechner, W. (2018). Guided Bone Regeneration with Collagen Membranes and Particulate Graft Materials: A Systematic Review and Meta-Analysis. *The International journal of oral & maxillofacial implants*, *33*(1), 87–100.

[52] Frost H. M. (1983). The regional acceleratory phenomenon: a review. *Henry Ford Hospital medical journal*, *31*(1), 3–9.

[53] Yaffe, A., Fine, N., & Binderman, I. (1994). Regional accelerated phenomenon in the mandible following mucoperiosteal flap surgery. *Journal of periodontology*, *65*(1), 79–83.

[54] Frost H. M. (1989). The biology of fracture healing. An overview for clinicians. Part I. *Clinical orthopaedics and related research*, (248), 283–293.

[55] Kole H. (1959). Surgical operations on the alveolar ridge to correct occlusal abnormalities. *Oral surgery, oral medicine, and oral pathology*, *12*(5).

[56] Generson, R. M., Porter, J. M., Zell, A., & Stratigos, G. T. (1978). Combined surgical and orthodontic management of anterior open bite using corticotomy. *Journal of oral surgery (American Dental Association : 1965)*, *36*(3), 216–219.

[57] Suya H. (1991) Corticotomy in orthodontics. In Hosl E, Baldauf A. (Eds.), Mechanical and biological basis in orthodontic therapy. *Germany Huthig Buch Verlag*: pp 207-26.

[58] Wilcko, W. M., Wilcko, T., Bouquot, J. E., & Ferguson, D. J. (2001). Rapid orthodontics with alveolar reshaping: two case reports of decrowding. *The International journal of periodontics & restorative dentistry*, *21*(1), 9–19.

[59] Vercellotti, T., & Podesta, A. (2007). Orthodontic microsurgery: a new surgically guided technique for dental movement. *The International journal of periodontics & restorative dentistry*, *27*(4), 325–331.

[60] Horton, J. E., Tarpley, T. M., Jr, & Wood, L. D. (1975). The healing of surgical defects in alveolar bone produced with ultrasonic instrumentation, chisel, and rotary bur. *Oral surgery, oral medicine, and oral pathology*, *39*(4), 536–546.

[61] Canullo, L., Peñarrocha, D., Peñarrocha, M., Rocio, A. G., & Penarrocha-Diago, M. (2014). Piezoelectric vs. conventional drilling in implant site preparation: pilot controlled randomized clinical trial with crossover design. *Clinical oral implants research*, *25*(12), 1336–1343.

[62] Fugito Junior, K., Cortes, A. R., de Carvalho Destro, R., & Yoshimoto, M. (2018). Comparative Study on the Cutting Effectiveness and Heat Generation of Rotary Instruments Versus Piezoelectric Surgery Tips Using Scanning Electron Microscopy and Thermal Analysis. *The International journal of oral & maxillofacial implants*, *33*(2), 345–350.

[63] Alikhani, M., Alikhani, M., Alansari, S., Almansour, A., Hamidaddin, M. A., Khoo, E., Lopez, J. A., Nervina, J. M., Nho, J. Y., Oliveira, S. M., Sangsuwon, C., & Teixeira, C. C. (2019). Therapeutic effect of localized vibration on alveolar bone of osteoporotic rats. *PloS one*, *14*(1), e0211004.

[64] Allen MR, Burr DB. Chapter 4 - Bone Modeling and Remodeling. In: Burr DB, Allen MR, eds. Basic and Applied Bone Biology. *Academic Press*; 2014:75-90.

[65] Duhamel, H. L. (1742). Sur le développement et la crue des os des animaux. *Mem Acad R Sci Paris*, *55*, 354-370.

[66] Owen, M. (1970). The origin of bone cells. *International review of cytology*, *28*, 213-238.

[67] Schepers, K., Pietras, E. M., Reynaud, D., Flach, J., Binnewies, M., Garg, T., ... & Passegué, E. (2013). Myeloproliferative neoplasia remodels the endosteal bone marrow niche into a self-reinforcing leukemic niche. *Cell stem cell*, *13*(3), 285-299.

[68] Misch, C. E. (2007). *Contemporary Implant Dentistry*. Elsevier Health Sciences.

[69] Le, B. Q., Nurcombe, V., Cool, S. M., Van Blitterswijk, C. A., De Boer, J., & LaPointe, V. L. S. (2017). The components of bone and what they can teach us about regeneration. *Materials*, *11*(1), 14.

[70] Batoon, L., Millard, S. M., Raggatt, L. J., & Pettit, A. R. (2017). Osteomacs and bone regeneration. *Current osteoporosis reports*, *15*(4), 385-395.

[71] Bar-Shavit, Z. (2007). The osteoclast: A multinucleated, hematopoietic-origin, bone-resorbing osteoimmune cell. *Journal of cellular biochemistry*, *102*(5), 1130-1139.

[72] Delgado-Calle, J., & Bellido, T. (2015). Osteocytes and skeletal pathophysiology. *Current molecular biology reports*, *1*(4), 157-167.

[73] Ohira, T., De Vit, A., & Dibart, S. (2019). Strategic use of ultrasonic frequencies for targeted bone bio-modification following piezoelectric bone surgery in rats (part I: early phase). *Int J Periodontics Restorative Dent*, *39*, 709-718.

[74] Florencio-Silva, R. GR d. *S. Sasso, E. Sasso-Cerri, MJ Simões, and PS Cerri,"Biology of bone tissue: structure, function, and factors that influence bone cells," BioMed Research International*, *2015*.

[75] Burr, David B., Matthew R. Allen. (2019) Basic and Applied Bone Biology. *Academic Press*, p 37-55.

[76] Copeland, B. (2022). Artificial Intelligence | Definition, Examples, and Applications. *Encyclopedia Britannica*. https://www.britannica.com/technology/artificial-intelligence.

[77] Buch, V. H., Ahmed, I., & Maruthappu, M. (2018). Artificial intelligence in medicine: current trends and future possibilities. *The British journal of general practice : the journal of the Royal College of General Practitioners*, *68*(668), 143–144.

[78] Bishop, Christopher. (2006). Pattern Recognition and Machine Learning. Information Science and Statistics. New York: Springer-Verlag. https://www.springer.com/gp/book/9780387310732.

[79] Chen, Y. Y., Lin, Y. H., Kung, C. C., Chung, M. H., & Yen, I. H. (2019). Design and Implementation of Cloud Analytics-Assisted Smart Power Meters Considering Advanced Artificial Intelligence as Edge Analytics in Demand-Side Management for Smart Homes. *Sensors (Basel, Switzerland)*, *19*(9), 2047.

[80] Wang, C. W., Huang, C. T., Lee, J. H., Li, C. H., Chang, S. W., Siao, M. J., Lai, T. M., Ibragimov, B., Vrtovec, T., Ronneberger, O., Fischer, P., Cootes, T. F., & Lindner, C. (2016). A benchmark for comparison of dental radiography analysis algorithms. *Medical image analysis*, *31*, 63–76.

[81] Wu, Y., Adeeb, S., & Doschak, M. R. (2015). Using Micro-CT Derived Bone Microarchitecture to Analyze Bone Stiffness - A Case Study on Osteoporosis Rat Bone. *Frontiers in endocrinology*, *6*, 80.

[82] Campbell, G. M., & Sophocleous, A. (2014). Quantitative analysis of bone and soft tissue by micro-computed tomography: applications to ex vivo and in vivo studies. *BoneKey Reports*, 3, 564.

[83] Zenzes, M., Zaslansky, P. (2021) Micro-CT data of early physiological cancellous bone formation in the lumbar spine of female C57BL/6 mice. *Sci Data* 8**,** 132.

[84] İsmail Alper İşoğlu, Nimet Bölgen, Petek Korkusuz, İbrahim Vargel, Hakan Hamdi Çelik, Emine Kılıç, Elif Güzel, Tarık Çavuşoğlu, Duygu Uçkan & Erhan Pişkin (2019). Stem cells combined 3D electrospun nanofibrous and macrochannelled matrices: a preliminary approach in repair of rat cranial bones, *Artificial Cells, Nanomedicine, and Biotechnology*, 47:1, 1094-1100

[85] Ronneberger, O., Fischer, P., & Brox, T. (2015). U-Net: Convolutional Networks for Biomedical Image Segmentation. *MICCAI*.

[86] Tassani, S., Korfiatis, V. and Matsopoulos, G.K. (2014), Influence of segmentation on micro-CT images of trabecular bone. *Journal of Microscopy*, 256: 75-81.

[87] Kang, Y., Engelke, K., & Kalender, W. A. (2003). A new accurate and precise 3-D segmentation method for skeletal structures in volumetric CT data. *IEEE transactions on medical imaging*, *22*(5), 586–598.

[88] Yang, R., & Yu, Y. (2021). Artificial Convolutional Neural Network in Object Detection and Semantic Segmentation for Medical Imaging Analysis. *Frontiers in oncology*, *11*, 638182.

[89] Ilesanmi, A.E., & Ilesanmi, T.O. (2021). Methods for image denoising using convolutional neural network: a review. *Complex & Intelligent Systems*, 1-20.

[90] Sarvamangala, D.R., Kulkarni, R.V. (2022) Convolutional neural networks in medical image understanding: a survey. *Evol. Intel.* 15, 1–22.

[91] Zeiler, Matthew D. (2012) ADADELTA: An Adaptive Learning Rate Method..*ArXiv*. 1212.

[92] Goodfellow, Ian, Yoshua Bengio, and Aaron Courville. (2016). Deep Learning. M*IT Press.*

[93] Parasuraman, S., Raveendran, R., & Kesavan, R. (2010). Blood sample collection in small laboratory animals. *Journal of pharmacology & pharmacotherapeutics*, *1*(2), 87–93.

[94] Goldman, H. M., & Smukler, H. (1978). Controlled surgical stimulation of periosteum. *Journal of periodontology*, *49*(10), 518–522.

[95] Kernitsky, J. R., Ohira, T., Shosho, D., Lim, J., Bamashmous, A., & Dibart, S. (2021). Corticotomy depth and regional acceleratory phenomenon intensity. *The Angle orthodontist*, *91*(2), 206–212.

[96] Anesi, A., Ferretti, M., Cavani, F., Salvatori, R., Bianchi, M., Russo, A., Chiarini, L., & Palumbo, C. (2018). Structural and ultrastructural analyses of bone regeneration in rabbit cranial osteotomy: Piezosurgery versus traditional osteotomes. *Journal of cranio-maxillo-facial surgery : official publication of the European Association for Cranio-Maxillo-Facial Surgery*, *46*(1), 107–118.

[97] Gyurko, Robert & Kim, S. & Dibart, S.. (2013). Nitric Oxide Mediates Piezotomy-Induced Increase in Bone Density. *J Dent Res*, 92 (Special Issue A), 2095.

CURRICULUM VITAE